

High Order Space-Time Finite Element Schemes for Acoustic and Viscodynamic Wave Equations with Temporal Decoupling*

H. T. Banks,[¶] Malcolm J Birch,[§] Mark P Brewin,^{||} Stephen E Greenwald,[‡]
Shuhua Hu,[¶] Zackary R Kenz,[¶] Carola Kruse,[†]
Matthias Maischak,[†] Simon Shaw,[†] John R Whiteman,[†]

June 12, 2013

*The work of Kruse, Shaw and Whiteman was supported by the Engineering and Physical Sciences research council EP/H011072/1. The work of Greenwald, Birch and Brewin was supported by the Engineering and Physical Sciences research council EP/H011285/1. The work of Banks, Hu and Kenz was supported, in part, by Grant Number R01AI071915-09 from the National Institute of Allergy and Infectious Diseases and also, in part, by the Air Force Office of Scientific Research under grant number AFOSR FA9550-12-1-0188. The work of Kenz was also supported, in part, by the Department of Education with a GAANN Fellowship under grant number P200A070386. All of this support is gratefully acknowledged.

[†]{carola.kruse|matthias.maischak|simon.shaw|john.whiteman}@brunel.ac.uk, BICOM, Brunel University, Uxbridge, UB8 3PH, England. www.brunel.ac.uk/bicom

[‡]s.e.greenwald@qmul.ac.uk, Blizard Institute, Barts and the London School of Medicine and Dentistry, Queen Mary, University of London, England.

[§]m.j.birch@qmul.ac.uk, Clinical Physics, Barts Health National Health Service Trust, England.

[¶]{htbanks|zrkenz|shu3}@ncsu.edu, Center for Research in Scientific Computation, North Carolina State University, Raleigh, NC 27695-8212, USA

^{||}mark.brewin@salisbury.nhs.uk, Salisbury District Hospital, England.

Abstract

We re-visit a method originally introduced by Werder et al. (in *Comput. Methods Appl. Mech. Engrg.*, 190:6685—6708, 2001) for discontinuous Galerkin finite element methods. In that approach block systems arise due to the coupling of the spatial systems through inner products of the temporal basis functions. If polynomials of degree r are used in time the block system has dimension $(r + 1)D$ and is usually regarded as being too large when $r > 1$. Werder *et al.* found that these matrices are diagonalizable over \mathbb{C} for $r \leq 100$. Hence, the time-coupled computations within a time step can be decoupled. Using either continuous Galerkin or spectral element methods in space, we apply this DG-in-time methodology, for the first time, to second order wave equations including elastodynamics with and without Kelvin-Voigt and Maxwell-Zener viscoelasticity. An example set of numerical results is given to demonstrate the favourable effect on error and computational work of the moderately high order (up to degree 7) temporal and spatio-temporal approximations, and we also touch on an application of this method to an ambitious problem related to the diagnosis of coronary artery disease.

Keywords: discontinuous Galerkin finite element method, spectral element method, space-time finite elements, high order methods, viscoelasticity

Sub. class: 65M60, 15A21, 35L10

Contents

1	Introduction and motivation	3
2	An abstract framework for decoupled DGFEM in time	5
3	Specific applications	10
3.1	The acoustic wave equation	10
3.2	Linear elasto- and viscodynamics	10
3.3	Alternative formulations with Kelvin-Voigt terms	13
3.4	Decoupling in the presence of viscoelastic damping	13
4	Numerical experiments	14
4.1	The acoustic wave equation	15
4.2	Elasto- and Visco-dynamics	21
5	Application: shear waves in biotissue-mimicking gel	21
6	Conclusions and discussion	34

1 Introduction and motivation

In 2001 Werder, Gerdes, Schötzau and Schwab, [43], formulated a space-time finite element method for the heat equation that employed a discontinuous Galerkin method in time. This was not the first such formulation (see e.g. [32]) but one particularly interesting feature of their work demonstrates that the temporal system can be diagonalised, thus making reasonably high order finite element time discretizations feasible. Also, there are recent results [1, 8] (see also the much earlier [10]) showing that high order spatial discretizations for wave equations are highly desirable in terms of the control of dispersion errors, and it is against this background that we aim here to extend the work of Werder *et al.* to facilitate high order space-time discretizations for second order hyperbolic wave equations. Our goal is to present a framework for useful and practical high order space-time finite element methods for a collection of common and important linear wave equation problems. We remark also that while high order time stepping has been around for some time, using Runge-Kutta methods for example, the approach below allows for the entire space-time discretization to be placed in a variational setting. This allows the arsenal of very powerful functional analytic tools relating to stability and error estimation to be deployed for the numerical simulation of wave propagation.

We deal first with an abstract formulation of the wave equation in Section 2 and describe the time discretization and its diagonalisation. We then apply this abstract framework to the specific examples of the acoustic wave equation and the equations of elasto- and viscodynamics in Section 3. The wave equation is dealt with rather swiftly in Subsection 3.1

and we move on to linear elasticity and Maxwell-Zener (hereditary) viscoelasticity in Subsection 3.2. With this we can then extend the formulation to deal with Kelvin-Voigt (or short-memory) viscoelasticity in, Subsection 3.3 and, finally, the decoupling procedure in the presence of both long- and short-memory viscoelasticity is described Subsection 3.4.

A collection of numerical results is given in Section 4 where we aim to demonstrate the convergence rates that are achieved in the natural norms associated with the wave equation. Our presentation is entirely practical in that we do not aim to establish theorems on error bounds but rather to demonstrate the practicality of high order finite element time stepping. Our motivation for adopting this methodology is to simulate waves in biotissue with a specific application related to the diagnosis of coronary artery disease. This application and the challenges it presents are outlined in Section 5. Section 6 then concludes with some observations.

Note that this is a shorter version of the long report in [34]. That longer report contains several appendices which contain some animated PDF's of the results from the problem described below in Section 5 (these are suited only to electronic viewing), and also a much more extensive set of numerical results illustrating convergence rates. Another appendix in that longer report also contains a discussion of the issue of solvers. For all of the numerical results given below we used Gaussian elimination, but acknowledge that in practice an iterative solver would often be desirable.

The approach to discretization taken below utilises a normalized Legendre basis to effect the *Discontinuous Galerkin Finite Element Method* (DGFEM)-in-time discretization while in space we use both continuous Galerkin and continuous spectral finite element methods on tensor product spaces. The former is implemented using high order Gauss-Legendre quadrature while the latter uses Gauss-Lobatto rules and nodes on tensor product spaces spanned by Lagrange basis functions, see e.g. [12, 17]. We recall that when using $d + 1$ integration points a Gauss-Legendre rule integrates polynomials of degree $2d + 1$ exactly while the Gauss-Lobatto rule only integrates those of degree $2d - 1$. Thus, although a non-negligible variational crime is committed, the spectral element method (SEM) using the Gauss-Lobatto rules has the advantage of producing diagonal mass matrices and allowing high order spatial discretization without needing 'p version' software. Also, although quadrilaterals and hexahedra can 'fill space' and fit boundaries just as easily as triangles and tetrahedra, we note that there are some polynomial degrees for which Lobatto-type rules exist on triangles, see [13, 15, 25, 45] and also the dispersion error study in [38], and so simplicial finite elements could also be used for high order mass lumping. We also note that if we used a spatially discontinuous finite element method then we could replace the Gauss-Lobatto rules and nodes with the higher order Gauss-Legendre rules because conformity (continuity at element boundaries) is no longer required. We also remark that for the implementations and numerical results given below both the Galerkin and spectral methods use Gauss-Lobatto nodes in the spatial mesh. This was purely for ease of implementation.

Irrespective of the use or not of the spectral finite element method, we shall see below (in (8) and (9)) that the decoupling procedure produces a set of boundary value problems that need to be solved for each time interval. Any suitable method could be employed here, including the standard Galerkin procedure, a 'blended procedure' as in [2], or indeed any of the many other tools that have been developed to 'solve' elliptic problems (including, if applicable, exact solutions and asymptotics).

Our notation is standard and, apart from these preliminaries, is introduced where necessary. Let the spatial domain of interest, Ω , be a time-independent open bounded polytope in \mathbb{R}^d for $d = 1, 2$ or 3 . We assume the boundary, $\partial\Omega$, is partitioned into $\{\Gamma_D, \Gamma_N\}$ (also time independent) and assume that Dirichlet boundary values are given on the closed set Γ_D with Neumann boundary values specified on the open (and possibly empty) set Γ_N . As usual we will insist that $\Gamma_D \cap \Gamma_N = \emptyset$ and $\Gamma_D \cup \Gamma_N = \partial\Omega$. We note that in general there exist problems for which Γ_D may have surface measure zero but here we insist that $\text{meas}_{\partial\Omega}(\Gamma_D) > 0$. Also, the unit outward normal vector to Γ_N will be written as $\hat{\mathbf{n}}$. To deal with the time dependence we set $I := (0, T]$ and will usually use overdots to denote partial time differentiation.

To provide some more context for what follows we recall that the idea of using Galerkin finite elements in space dates back to [16] and [42] and, of course, is now a method of choice in the vast majority of cases involving elliptic operators. However, although given much less exposure, the idea of using Galerkin discretizations in time is also not new (e.g. [28, 29, 46]) although it seems clear that these methods never really caught the imagination of users and producers of codes until much more recently. In fact, arguably, it was the work of Eriksson and Johnson, see [18], on adaptive space-time formulations for parabolic problems that seemed to have revived interest in these methods. The formulations in [14, 20, 26, 27, 36] are closely related but here we stay much closer to the crisper formulation given by Johnson in [33]. Although not relevant to our needs here we note that there also exist continuous Galerkin methods for time discretization (e.g. [3, 21] and [24]).

We close this introduction by recalling one very basic reason why high order schemes are useful. Suppose we compute up to time T using $N_1 \gg 1$ time steps. If piecewise polynomial degree r_1 is used for the approximation then on each step we can expect the error to be of the order $N_1^{-d_1}$ where $d_1 = r_1 + 1$. We will see below that d_1 matrix solves are required on each time interval and so if we (simplistically) assume that the solver time is constant in the time discretization parameters the amount of computational work, as measured by the total number of solves, is $N_1 d_1$. Now consider another set up with $N_2 > N_1$ and with polynomials of degree r_2 . Setting $d_2 = r_2 + 1$ and asking that the errors be ‘the same’ we have $N_1^{d_1} = N_2^{d_2}$ so that $N_2 = N_1^\gamma$ for $\gamma = d_1/d_2 = (\ln N_2)/(\ln N_1)$. Since $N_2 > N_1 \gg 1$ we must have that $\gamma > 1$ which, of course, means that fewer time steps are required for higher degree polynomials. The ratio of computational work needed is then $N_1 d_1 / N_2 d_2 = \gamma N_1^{1-\gamma} \ll 1$ as N_1 and/or γ become large and so we conclude that higher order schemes are capable of providing higher fidelity solutions than lower order schemes for the same amount of computational work. We attempt to illustrate this later for the 2D examples in Section 5.

2 An abstract framework for decoupled DGFEM in time

Before getting to the specific formulations of the later sections we first introduce an abstract formulation along with a semidiscrete time-discretization using the DGFEM. To this end we let $V \hookrightarrow H \hookrightarrow V'$ be a Gelfand triple of reflexive Hilbert spaces (dense and continuous embeddings, see, e.g., Wloka [44]) and denote the inner product and norm on H by $(\cdot, \cdot): H \times H \rightarrow \mathbb{R}$ and $\|\cdot\| = (\cdot, \cdot)^{1/2}$. We deal in this section with the standard abstract form of second-order wave equation problems in order to fix ideas and notation. Later, in Section 3

we recall some concrete applications and also some damping terms. These are important for the soft-tissue applications that we have in mind (see later in Section 5).

Let $a: V \times V \rightarrow \mathbb{R}$ be a symmetric and V -coercive bilinear form and assume that, for almost every $t \in I$, we are given data $L(t): I \rightarrow V'$. Introducing $w := \dot{u}$ and suppressing spatial dependence for clarity we consider the abstract problem of finding a smooth map $u: I \rightarrow V$ such that,

$$(\varrho \dot{w}(t), v) + a(u(t), v) = \langle L(t), v \rangle \quad \forall v \in V, \quad (1)$$

$$u(0) = \check{u} \quad \text{and} \quad \dot{u}(0) = \check{w}, \quad (2)$$

where $\langle \cdot, \cdot \rangle: V' \times V \rightarrow \mathbb{R}$ denotes the duality pairing arising from the continuous extension of $(\cdot, \cdot)_H$ to $V' \times V$ and \check{u}, \check{w} are initial data. For convenience and the avoidance of unimportant constants we henceforth consider the space V as equipped with the scalar product $a(\cdot, \cdot)$ and the induced norm $\| \cdot \|_V = a(\cdot, \cdot)^{1/2}$. In this ϱ is a known positive-valued function, often a constant, which in solid dynamics represents the material's mass density. Also, and as is usual for time dependent problems, for a Banach space $(\mathcal{B}, \| \cdot \|_{\mathcal{B}})$ we define the $L_p(0, t; \mathcal{B})$ norms by $\| \mathbf{v} \|_{L_p(0, t; \mathcal{B})} := \| \| \mathbf{v}(\cdot) \|_{\mathcal{B}} \|_{L_p(0, t)}$. The DG-in-time formulation that follows is identical to that given by Johnson in [33].

Discretizing the time interval so that $0 = t_0 < t_1 < \dots < t_N = T$, defining the time step $k_n := t_n - t_{n-1}$ and setting $I_n := (t_{n-1}, t_n)$ we define, as usual, the jump notation,

$$[[w]]_n := w_n^+ - w_n^- \quad \text{where} \quad w_n^\pm := \lim_{s \downarrow 0} w(t_n \pm s).$$

The semidiscrete DGFEM approximation of (1) is then: for each $n = 1, 2, \dots, N$ in turn, find $(U, W)|_{I_n} \in \mathbb{P}_r(I_n; V) \times \mathbb{P}_r(I_n; V)$ such that

$$\begin{aligned} & \int_{I_n} (\varrho \dot{W}(t), \vartheta(t)) + a(U(t), \vartheta(t)) dt + (\varrho [[W]]_{n-1}, \vartheta_{n-1}^+) + a([[U]]_{n-1}, \zeta_{n-1}^+) \\ & + \int_{I_n} a(\dot{U}(t), \zeta(t)) - a(W(t), \zeta(t)) dt = \int_{I_n} \langle L(t), \vartheta(t) \rangle dt \\ & \forall \vartheta \in \mathbb{P}_r(I_n; V) \quad \text{and} \quad \forall \zeta \in \mathbb{P}_r(I_n; V), \end{aligned} \quad (3)$$

with the understanding that $U_0^- := \check{u}$ and $W_0^- := \check{w}$. Here, for each n , we use $\mathbb{P}_r(I_n; X)$ to denote the space of polynomials of degree r on the time interval I_n with coefficients in the target space X . The target space is omitted when $X = \mathbb{R}$ and we note that r could be n -dependent, but we do not need to dwell on that here. Choosing $\vartheta = W$ and $\zeta = U$ gives,

$$\begin{aligned} & \| \varrho^{1/2} W_n^- \|^2 + \| \varrho^{1/2} W_{n-1}^+ \|^2 - 2(\varrho W_{n-1}^-, W_{n-1}^+) + \| U_n^- \|_V^2 + \| U_{n-1}^+ \|_V^2 - 2a(U_{n-1}^-, U_{n-1}^+) \\ & = \int_{I_n} \frac{d}{dt} (\| \varrho^{1/2} W(t) \|^2 + \| U(t) \|_V^2) dt + 2(\varrho [[W]]_{n-1}, W_{n-1}^+) + 2a([[U]]_{n-1}, U_{n-1}^+) \\ & = 2 \int_{I_n} (\varrho \dot{W}(t), W(t)) + a(\dot{U}(t), U(t)) dt + 2(\varrho [[W]]_{n-1}, W_{n-1}^+) + 2a([[U]]_{n-1}, U_{n-1}^+) \\ & = 2 \int_{I_n} \langle L(t), W(t) \rangle dt, \end{aligned}$$

and since

$$\begin{aligned} & \| \varrho^{1/2} W_n^- \|^2 + \| \varrho^{1/2} W_{n-1}^+ \|^2 - 2(\varrho W_{n-1}^-, W_{n-1}^+) \\ & = \| \varrho^{1/2} W_n^- \|^2 - \| \varrho^{1/2} W_{n-1}^- \|^2 + \| [\varrho^{1/2} W]_{n-1} \|^2 \end{aligned}$$

we arrive at

$$\begin{aligned} & \|\varrho^{1/2}W_n^-\|^2 - \|\varrho^{1/2}W_{n-1}^-\|^2 + \|[\varrho^{1/2}W]_{n-1}\|^2 \\ & \quad + \|U_n^-\|_V^2 - \|U_{n-1}^-\|_V^2 + \|[U]_{n-1}\|_V^2 = 2 \int_{I_n} \langle L(t), W(t) \rangle dt. \end{aligned}$$

Taking $L = 0$ and summing over $n = 1, \dots, N$ then gives the basic stability estimate,

$$\|\varrho^{1/2}W_N^-\|^2 + \|U_N^-\|_V^2 + \sum_{i=1}^N \left(\|[\varrho^{1/2}W]_{n-1}\|^2 + \|[U]_{n-1}\|_V^2 \right) = \|\varrho^{1/2}\check{w}\|^2 + \|\check{u}\|_V^2,$$

and reminds us that this scheme is dissipative. This, of course, is a general statement and holds for all polynomial degrees. It is also useful at this stage to recall Claes Johnson's result in [33] which focussed on Galerkin schemes using discontinuous piecewise linears in time and continuous piecewise linears in space for the standard problem $\ddot{u} - \nabla^2 u = f$ subject to homogeneous Dirichlet boundary data. Although the presentation of the *a priori* error bound there is rather terse it seems from the comments below it and in the introduction that we can expect the following,

$$\|w(t_N) - W_N^-\| + \|u(t_N) - U_N^-\|_V \leq C(hk^{-1/2} + k^3), \quad (4)$$

$$\|u(t_N) - U_N^-\| \leq C(h^2k^{-1/2} + k^3), \quad (5)$$

so long as the space-mesh is kept constant in time and where h is the spatial mesh size and k the constant time step. We will give some demonstration of these expected convergence rates later, for linear as well as higher degree approximations, but now move on to the specifics of the implementation.

Let $\{\phi_i : i = 0, 1, \dots, r\}$ be a basis for $\mathbb{P}_r(I_n)$ and introduce the ansatz forms of the approximations to u and w on I_n as,

$$U(t)|_{I_n} = \sum_{j=0}^r \phi_j(t)U_j \quad \text{and} \quad W(t)|_{I_n} = \sum_{j=0}^r \phi_j(t)W_j$$

where $\{U_0, U_1, \dots\}, \{W_0, W_1, \dots\} \subseteq V$. Replacing each of $\vartheta(t)$ and $\zeta(t)$ with $\phi_i(t)\vartheta$ for $\phi_i \in \mathbb{P}_r(I_n)$ and $\vartheta \in V$ in (3) we obtain first,

$$\begin{aligned} & \sum_{j=0}^r \int_{I_n} \dot{\phi}_j(t)\phi_i(t)(\varrho W_j, \vartheta) + \phi_j(t)\phi_i(t)a(U_j, \vartheta) dt \\ & + \sum_{j=0}^r \phi_{j,n-1}^+ \phi_{i,n-1}^+ (\varrho W_j, \vartheta) = \int_{I_n} \phi_i(t)\langle L(t), \vartheta \rangle dt + \phi_{i,n-1}^+ (\varrho W_{n-1}^-, \vartheta) \end{aligned}$$

and second,

$$\begin{aligned} & \sum_{j=0}^r \int_{I_n} \dot{\phi}_j(t)\phi_i(t)a(U_j, \vartheta) - \phi_j(t)\phi_i(t)a(W_j, \vartheta) dt \\ & + \sum_{j=0}^r \phi_{j,n-1}^+ \phi_{i,n-1}^+ a(U_j, \vartheta) = \phi_{i,n-1}^+ a(U_{n-1}^-, \vartheta) \end{aligned}$$

where each holds for all $\vartheta \in V$ and for each $i \in \{0, 1, \dots, r\}$. Define matrices via,

$$\mathbf{A}_{ij} := \int_{I_n} \dot{\phi}_j(t)\phi_i(t) dt + \phi_{j,n-1}^+\phi_{i,n-1}^+ \quad \text{and} \quad \mathbf{M}_{ij} := \int_{I_n} \phi_j(t)\phi_i(t) dt,$$

where i indexes the rows, and then by choosing our basis functions as the image under the linear map from $[-1, 1]$ to I_n of the normalized Legendre polynomials we conclude easily that $2\mathbf{M} = k_n\mathbf{I}$. It seems useful at this point to recall the remark in [43] that these matrices are hierarchical, and also that they can be precomputed just once on a reference length and then re-used for subsequent computations.

However, the main point and motivation for us here is that Werder *et al.* in [43] report that \mathbf{A} is diagonalizable over \mathbb{C} for all polynomial degrees of practical interest. This in particular means that the computational linear algebra associated with these objects is relatively cheap, and it also allows us to write $\mathbf{D} = \mathbf{Q}^{-1}\mathbf{A}\mathbf{Q} = \lceil \lambda_1 \cdots \lambda_{r+1} \rceil$ where $\lceil \cdots \rceil$ indicates a diagonal matrix of pairwise complex conjugate eigenvalues and where \mathbf{Q} has complex entries.

So, proceeding step by step, and using the summation convention, our system is

$$\mathbf{A}_{ij}(\varrho W_j, \vartheta) + \delta_{ij} \frac{k_n}{2} a(U_j, \vartheta) = \mathbf{F}_i(\vartheta), \quad (6)$$

$$\mathbf{A}_{ij}a(U_j, \vartheta) - \delta_{ij} \frac{k_n}{2} a(W_j, \vartheta) = \mathbf{G}_i(\vartheta), \quad (7)$$

where

$$\mathbf{F}_i(\vartheta) := \int_{I_n} \phi_i(t)\langle L(t), \vartheta \rangle dt + \phi_{i,n-1}^+(\varrho W_{n-1}^-, \vartheta) \quad \text{and} \quad \mathbf{G}_i(\vartheta) := \phi_{i,n-1}^+ a(U_{n-1}^-, \vartheta)$$

are known from data and the previous time step. Defining $\{Y_q\}$ and $\{Z_q\}$ as the unique solutions of $W_j = \mathbf{Q}_{jq}Y_q$ and of $U_j = \mathbf{Q}_{jq}Z_q$ we have,

$$\mathbf{A}_{ij}\mathbf{Q}_{jq}(\varrho Y_q, \vartheta) + \delta_{ij} \frac{k_n}{2} \mathbf{Q}_{jq}a(Z_q, \vartheta) = \mathbf{F}_i(\vartheta),$$

$$\mathbf{A}_{ij}\mathbf{Q}_{jq}a(Z_q, \vartheta) - \delta_{ij} \frac{k_n}{2} \mathbf{Q}_{jq}a(Y_q, \vartheta) = \mathbf{G}_i(\vartheta),$$

and taking linear combinations using the rows of $\mathbf{R} := \mathbf{Q}^{-1}$ then yields,

$$\mathbf{R}_{pi}\mathbf{A}_{ij}\mathbf{Q}_{jq}(\varrho Y_q, \vartheta) + \frac{k_n}{2}\mathbf{R}_{pi}\delta_{ij}\mathbf{Q}_{jq}a(Z_q, \vartheta) = \mathbf{R}_{pi}\mathbf{F}_i(\vartheta),$$

$$\mathbf{R}_{pi}\mathbf{A}_{ij}\mathbf{Q}_{jq}a(Z_q, \vartheta) - \frac{k_n}{2}\mathbf{R}_{pi}\delta_{ij}\mathbf{Q}_{jq}a(Y_q, \vartheta) = \mathbf{R}_{pi}\mathbf{G}_i(\vartheta).$$

Noting that $\mathbf{R}_{pi}\mathbf{A}_{ij}\mathbf{Q}_{jq} = \delta_{pq}\lambda_p$ and $\mathbf{R}_{pi}\delta_{ij}\mathbf{Q}_{jq} = \delta_{pq}$, setting $F_i(\vartheta) := \mathbf{R}_{ip}\mathbf{F}_p(\vartheta)$ and $G_i(\vartheta) := \mathbf{R}_{ip}\mathbf{G}_p(\vartheta)$ we now arrive at the decoupled form with **summation no longer implied**,

$$2\lambda_i(\varrho Y_i, \vartheta) + k_n a(Z_i, \vartheta) = 2F_i(\vartheta),$$

$$2\lambda_i a(Z_i, \vartheta) - k_n a(Y_i, \vartheta) = 2G_i(\vartheta).$$

Therefore, defining $\beta_i := \Sigma_p \mathbf{R}_{ip}\phi_{p,n-1}^+$,

$$4\lambda_i^2(\varrho Y_i, \vartheta) + k_n^2 a(Y_i, \vartheta) = 4\lambda_i F_i(\vartheta) - 2k_n G_i(\vartheta), \quad (8)$$

$$a(2\lambda_i Z_i - k_n Y_i - 2\beta_i U_{n-1}^-, \vartheta) = 0, \quad (9)$$

since $2G_i(\vartheta) = 2\beta_i a(U_{n-1}^-, \vartheta)$.

The algorithm is now clear. At each time step we solve $r+1$ boundary value problems for the complex unknowns $\{Y_i\}_{i=0}^r$ and then update with $Z_i = (2\lambda_i)^{-1}(k_n Y_i + 2\beta_i U_{n-1}^-)$. We recall that for the SEM the mass matrices arising from the spatial discretization of these systems are diagonal, and note also that since λ_i^2 is complex we will either need to introduce complex arithmetic in the solver or treat the complex system as a two-by-two-block real system.

Remark 2.1 (non-zero Dirichlet data) *Although not included in the formulation above, some of the examples below use non-zero Dirichlet boundary data. These data are imposed by time-projection on to the temporal basis at each desired $\mathbf{x} \in \Gamma_D$ to determine pointwise boundary values for each of the decoupled systems. Specifically, suppose that we want to set the known Dirichlet value $w^D(t) \equiv \dot{u}^D(t)$ during the time interval I_n . We assume the ansatz $w^D(t) = \sum_{j=0}^r \phi_j(t) w_j^D$ (with the superscript D denoting ‘Dirichlet’) and then determine the w_j^D by the projection:*

$$\int_{I_n} w^D(t) \phi_i(t) dt = \sum_{j=0}^r w_j^D \int_{I_n} \phi_j(t) \phi_i(t) dt = \frac{k_n}{2} w_j^D.$$

We then do the same for the U_j^D values at the boundary and we modify (6) to become,

$$\mathbf{A}_{ij}(\varrho W_j^I, \vartheta) + \delta_{ij} \frac{k_n}{2} a(U_j^I, \vartheta) = \mathbf{F}_i(\vartheta) - \mathbf{A}_{ij}(\varrho W_j^D, \vartheta) - \delta_{ij} \frac{k_n}{2} a(U_j^D, \vartheta), \quad (10)$$

where $W_{n-1}^- = (W_{n-1}^-)^I + (W_{n-1}^-)^D$ is now used in the definition of \mathbf{F}_i , and the superscript I denotes ‘interior’. The W_j^D and U_j^D on the right are then spatially interpolated along the boundary by augmenting the spatial basis to incorporate the Dirichlet boundary nodes (with zero values in the interior), and then ‘mass’ and ‘stiffness’ (rectangular-) matrix-vector contributions to the load are formed from these new inner products on the right hand side of (10). Since we derive the boundary values for w from \dot{u} they cancel each other out in (7) and so no change is needed there. The remainder of the implementation is as described earlier but with the ‘interior’ functions being the unknowns.

Remark 2.2 *We could also define the semidiscrete DGFEM approximation of (1) as: for each $n = 1, 2, \dots, N$ in turn, find $(U, W)|_{I_n} \in \mathbb{P}_r(I_n; V) \times \mathbb{P}_r(I_n; V)$ such that*

$$\begin{aligned} & \int_{I_n} (\varrho \dot{W}(t), \vartheta(t)) + a(U(t), \vartheta(t)) dt + (\varrho \llbracket W \rrbracket_{n-1}, \vartheta_{n-1}^+) + (\varrho \llbracket U \rrbracket_{n-1}, \zeta_{n-1}^+) \\ & + \int_{I_n} (\varrho \dot{U}(t), \zeta(t)) - (\varrho W(t), \zeta(t)) dt = \int_{I_n} \langle L(t), \vartheta(t) \rangle dt \\ & \forall \vartheta \in \mathbb{P}_r(I_n; V), \mathbb{P}_r(I_n; H). \end{aligned} \quad (11)$$

The advantage of this is that we could deal with pure Neumann problems wherein $a(\cdot, \cdot)$ may no longer be coercive. Numerical tests show that this scheme works well but we are not able to prove any stability estimates for it. For that reason we do not consider it further here, but note that the time decoupling method described above could be applied to this formulation also.

3 Specific applications

In this section we apply the foregoing to the specific examples of the wave equation and elastodynamics. We also enhance the formulation to take viscoelastic damping effects into account.

3.1 The acoustic wave equation

In this subsection we consider the specific example problem where we seek u such that,

$$\begin{aligned} \dot{w} - c^2 \nabla^2 u &= f, \\ w &= \dot{u}, \quad u(0) = \check{u}, \quad w(0) = \check{w}, \\ u &= 0 \text{ on } \Gamma_D \times I \quad \text{and} \quad c^2 \nabla u \cdot \hat{\mathbf{n}} = g \text{ on } \Gamma_N \times I. \end{aligned}$$

Defining $a(w, v) := (c^2 \nabla w, \nabla v)$, where (\cdot, \cdot) is the $L_2(\Omega)$ inner product, and setting $V := \{v \in H^1(\Omega) : v|_{\Gamma_D} = 0\}$ the weak form of the problem is: find $u : I \rightarrow V$ such that,

$$(\dot{w}, \phi) + a(\nabla u, \nabla \phi) + a(\dot{u} - w, \psi) = \langle L(t), \phi \rangle \quad \forall \phi, \psi \in V$$

where $\langle L(t), \phi \rangle := (f, \phi) + (g, \phi)_{\Gamma_N}$. Notice that we overload (\cdot, \cdot) in a completely standard way where no notational distinction is made when the arguments are scalar- or vector-valued.

The semidiscrete finite element formulation in (3) applies without change and so on the n -th time step, of width $k_n = t_n - t_{n-1}$ say, and for $i = 0, \dots, r$, we have to solve the boundary value problems given by:

$$(Y_i, \vartheta) + \kappa_i a(Y_i, \vartheta) = \ell_i(\vartheta) \quad \forall \vartheta \in V,$$

where $\kappa_i := \frac{1}{4}(k_n/\lambda_i)^2$, and perform the update $Z_i = (2\lambda_i)^{-1}(k_n Y_i + 2\beta_i U_{n-1}^-)$. Once done we obtain $W_i = \Sigma_j \mathbf{Q}_{ij} Y_j$ and $U_i = \Sigma_j \mathbf{Q}_{ij} Z_j$. In these $\ell_i(\vartheta) := (4\lambda_i F_i(\vartheta) - 2k_n G_i(\vartheta))/4\lambda_i^2$, $F_i(\vartheta) = \Sigma_j \mathbf{Q}_{ij}^{-1} \mathbf{F}_j(\vartheta)$ and $G_i(\vartheta) = \Sigma_j \mathbf{Q}_{ij}^{-1} \mathbf{G}_j(\vartheta)$ where

$$\mathbf{F}_i(\vartheta) = \int_{I_n} \phi_i(t) \langle L(t), \vartheta \rangle dt + \phi_{i,n-1}^+ (\varrho W_{n-1}^-, \vartheta) \quad \text{and} \quad \mathbf{G}_i(\vartheta) = \phi_{i,n-1}^+ a(U_{n-1}^-, \vartheta).$$

The spatial discretization has already been described in general terms earlier in Section 1 and so all that remains is to demonstrate the behaviour of the scheme. This is done later in Subsection 4.1 for both 1D and 2D test problems. In those experiments we will have either $c^2 = E_0/\varrho$ or $c^2 = G/\varrho$ where E_0 and G represent stiffness moduli and ϱ a mass density (see Section 5).

3.2 Linear elasto- and viscodynamics

In this section we suppose that Ω represents the interior of a linear viscoelastic compressible body. This body is acted upon by a system of body forces $\mathbf{f} := (f_i(\mathbf{x}, t))_{i=1}^d$ for $\mathbf{x} := (x_i)_{i=1}^d \in \Omega$ and $t \in I$ and on the open (and possibly empty) set Γ_N there is prescribed a system of surface tractions $\mathbf{g} := (g_i(\mathbf{x}, t))_{i=1}^d$ for $\mathbf{x} \in \Gamma_N$ and $t \in I$.

The displacement from equilibrium resulting from the action of the applied forces \mathbf{f} and \mathbf{g} is denoted by $\mathbf{u} = (u_i)_{i=1}^d: \Omega \times I \rightarrow \mathbb{R}^d$ and in this linear theory the deformation is described by the strain tensor $\boldsymbol{\varepsilon} := (\varepsilon_{ij})_{i,j=1}^d$ given by,

$$\varepsilon_{ij}(\mathbf{u}) := \frac{1}{2} \left(\frac{\partial u_i}{\partial x_j} + \frac{\partial u_j}{\partial x_i} \right). \quad (12)$$

We assume also that $t = 0$ is a reference time such that $\mathbf{u} = \mathbf{0}$ for all $t < 0$.

Newton's second law of motion with boundary conditions gives for each $i \in \{1, \dots, d\}$ that,

$$\begin{aligned} \rho \dot{w}_i - \sigma_{ij,j} &= f_i & \text{in } \Omega \times I, \\ \mathbf{w} &= \dot{\mathbf{u}}, & \mathbf{u}(0) = \check{\mathbf{u}}, & \mathbf{w}(0) = \check{\mathbf{w}} \\ \mathbf{u} &= \mathbf{0} \text{ on } \Gamma_D \times I & \text{and} & \sigma_{ij} \hat{n}_j = g_i \text{ on } \Gamma_N \times I \end{aligned} \quad (13)$$

with summation implied and where $\boldsymbol{\sigma} := (\sigma_{ij})_{i,j=1}^d$ is the symmetric stress tensor.

We close this problem by recalling the standard literature on viscoelasticity (e.g. [23, 19]) and introduce the following linear hereditary viscoelastic constitutive relationship between stress and strain,

$$\sigma_{ij}(\mathbf{u}; t) = C_{ijkl} \varepsilon_{kl}(\dot{\mathbf{u}}(t)) + D_{ijkl}(0) \varepsilon_{kl}(\mathbf{u}(t)) - \int_0^t \frac{\partial D_{ijkl}(t-s)}{\partial s} \varepsilon_{kl}(\mathbf{u}(s)) ds \quad (14)$$

where, as usual, we omit the \mathbf{x} dependence. In this \mathbf{C} and $\mathbf{D}(t)$ are fourth order tensors with \mathbf{C} related to the Kelvin-Voigt model of viscoelasticity and $\mathbf{D}(t)$ stemming from the Zener and Maxwell models. Although retained for the sake of generality, we could just assume that $\mathbf{C} = \mathbf{0}$ because (discussed later in Section 3.3) the case $\mathbf{C} \neq \mathbf{0}$ can be formulated in a way that can be dealt with by the method described by Werder *et al.* in [43], with the internal variable augmentation as described below.

The *Hooke's law tensor* $\mathbf{D}(t) := (D_{ijkl}(t))_{i,j,k,l=1}^d$ is a fourth-order stress relaxation tensor satisfying the following symmetries:

$$D_{ijkl}(t) = D_{jikl}(t) = D_{ijlk}(t) \quad \text{but, in general,} \quad D_{ijkl}(t) \neq D_{klij}(t). \quad (15)$$

However, we do have $D_{ijkl}(t) = D_{klij}(t)$ for $t = 0$ and $t = \infty$ in general, and for all t for isotropic materials (see e.g. [37, equations (1.10), (2.62)]), and the components of \mathbf{D} can be assumed to be (a.e. in Ω) of class W_∞^1 in t although we will not need this level of generality. In addition, since $\mathbf{D}(0)$ measures instantaneous linear elastic response we follow Hooke's law and assume positive-definiteness: $\gamma_{ij} \gamma_{kl} D_{ijkl}(0) > 0$ a.e. in Ω for all non-zero symmetric second order tensors $\boldsymbol{\gamma}$.

In what follows we will assume a much simpler version of this constitutive law. First we assume that the material is *synchronous* so that $\mathbf{D}(t)$ is replaced by $\varphi(t)\mathbf{D}$ where \mathbf{D} is now constant in time and φ is a stress relaxation function. Following classical theory we assume the Prony series form,

$$\varphi(t) = \varphi_0 + \sum_{q=1}^{N_\varphi} \varphi_q \exp(-t/\tau_q) \quad (16)$$

where $\varphi_q \geq 0$ for $q \in \{0, 1, \dots, N_\varphi\}$, $\tau_q > 0$ for $q \in \{1, \dots, N_\varphi\}$ and we normalize so that $\varphi(0) = \varphi_0 + \sum_q \varphi_q = 1$. The case $\varphi_0 = 0$ corresponds to a viscoelastic fluid in the

sense described by Golden and Graham in [23] whereas $\varphi_0 > 0$ gives a solid. The second assumption is that the material is homogenous and so, in particular, is isotropic. This means that \mathbf{D} can be described by just two independent *Lamé coefficients* denoted, usually, by $\lambda = \nu E / ((1 + \nu)(1 - 2\nu))$ and $\mu = 2G = E / (1 + \nu)$ where E is Young's modulus, G is the shear modulus and ν is Poisson's ratio. Theoretically $\nu \in (-1, 1/2]$ but because we are dealing only with compressible non-auxetic materials we have $\nu \in (0, 1/2)$ and both λ and μ are well defined. The action of \mathbf{D} is now given specifically by $D_{ijkl}\varepsilon_{kl}(\mathbf{u}) = \lambda \nabla \cdot \mathbf{u} \delta_{ij} + \mu \varepsilon_{ij}(\mathbf{u})$ and the constitutive law can be written in the form,

$$\begin{aligned} \boldsymbol{\sigma}(\mathbf{u}; t) &= \mathbf{C}\boldsymbol{\varepsilon}(\dot{\mathbf{u}}(t)) + \mathbf{D} \left(\boldsymbol{\varepsilon}(\mathbf{u}(t)) - \int_0^t \varphi_s(t-s) \boldsymbol{\varepsilon}(\mathbf{u}(s)) ds \right), \\ &= \mathbf{C}\boldsymbol{\varepsilon}(\dot{\mathbf{u}}(t)) + \mathbf{D}\boldsymbol{\varepsilon} \left(\mathbf{u}(t) - \sum_{q=1}^{N_\varphi} \int_0^t \frac{\varphi_q}{\tau_q} e^{-(t-s)/\tau_q} \mathbf{u}(s) ds \right), \\ &= \mathbf{C}\boldsymbol{\varepsilon}(\dot{\mathbf{u}}(t)) + \mathbf{D}\boldsymbol{\varepsilon} \left(\mathbf{u}(t) - \sum_{q=1}^{N_\varphi} \mathbf{u}_q^*(t) \right), \end{aligned}$$

where for $q = 1, 2, \dots, N_\varphi$,

$$\mathbf{u}_q^*(t) := \int_0^t \frac{\varphi_q}{\tau_q} e^{-(t-s)/\tau_q} \mathbf{u}(s) ds$$

are *internal variables* (see, for example, [6, 22, 30, 31]) and satisfy,

$$\tau_q \dot{\mathbf{u}}_q^* + \mathbf{u}_q^* = \varphi_q \mathbf{u} \quad \text{with} \quad \mathbf{u}_q^*(0) = \mathbf{0}. \quad (17)$$

To give a weak formulation of this problem we first define the product Hilbert spaces, $\mathbf{H}^s(\Omega) := H^s(\Omega)^n$, for $s = 0, 1, 2, \dots$, with inner products given for all $\boldsymbol{\chi}, \mathbf{v} \in \mathbf{H}^s(\Omega)$ by $(\boldsymbol{\chi}, \mathbf{v})_s := \sum_{i=1}^d (\chi_i, v_i)_{H^s(\Omega)}$. These spaces have the natural norms $\|\cdot\|_s := \sqrt{(\cdot, \cdot)_s}$ and, of course, $\mathbf{L}_2(\Omega) \equiv \mathbf{H}^0(\Omega)$. We also use the (symmetric second order) tensor-valued L_2 space,

$$\mathbf{L}_2(\Omega) := \{ \boldsymbol{\gamma} = (\gamma_{ij})_{i,j=1}^d : \gamma_{ij} = \gamma_{ji} \in L_2(\Omega) \forall i, j \in \{1, \dots, d\} \}$$

and, noting the essential boundary condition, we define the test space as,

$$V := \left\{ \mathbf{v} \in \mathbf{H}^1(\Omega) : \mathbf{v} = \mathbf{0} \text{ on } \Gamma_D \right\}. \quad (18)$$

After integration by parts (see e.g. [41] for details) we then arrive at the weak problem of seeking a smooth map, $\mathbf{u}: I \rightarrow V$, such that,

$$(\rho \dot{\mathbf{u}}(t), \mathbf{v}) + a(\mathbf{u}(t), \mathbf{v}) + b(\dot{\mathbf{u}}(t), \mathbf{v}) = \langle L(t), \mathbf{v} \rangle + \sum_{q=1}^{N_\varphi} a(\mathbf{u}_q^*(t), \mathbf{v}) \quad \forall \mathbf{v} \in V, \quad (19)$$

$$a(\tau_q \dot{\mathbf{u}}_q^*(t) + \mathbf{u}_q^*(t), \mathbf{v}) = a(\varphi_q \mathbf{u}(t), \mathbf{v}) \quad \text{for } q = 1, \dots, N_\varphi \text{ and } \forall \mathbf{v} \in V. \quad (20)$$

Here the bilinear forms $a, b: H \times H \rightarrow \mathbb{R}$ are defined by

$$a(\boldsymbol{\chi}, \mathbf{v}) := \int_{\Omega} D_{ijkl}(0) \varepsilon_{kl}(\boldsymbol{\chi}) \varepsilon_{ij}(\mathbf{v}) d\Omega \quad \text{and} \quad b(\boldsymbol{\chi}, \mathbf{v}) := \int_{\Omega} C_{ijkl} \varepsilon_{kl}(\boldsymbol{\chi}) \varepsilon_{ij}(\mathbf{v}) d\Omega$$

for all $\boldsymbol{\chi}, \mathbf{v} \in H$, and $L: I \rightarrow V'$ is the time dependent linear form defined through,

$$\langle L(t), \mathbf{v} \rangle := \int_{\Omega} \mathbf{v} \cdot \mathbf{f}(t) d\Omega + \oint_{\Gamma_N} \mathbf{v} \cdot \mathbf{g}(t) d\Gamma \quad \forall \mathbf{v} \in H.$$

This completes the statement of the basic problem. The next section discusses an alternative approach which seems attractive when the Kelvin-Voigt tensor is positive definite, and the section after describes the extension of the decoupling procedure to incorporate the viscoelastic terms that have just been introduced.

3.3 Alternative formulations with Kelvin-Voigt terms

If the Kelvin-Voigt tensor, \mathbf{C} , is positive definite then in (13) we can set $\mathbf{w} = \dot{\mathbf{u}}$ and integrate by parts in (14) to obtain,

$$\sigma_{ij}(\mathbf{w}; t) = C_{ijkl} \varepsilon_{kl}(\mathbf{w}(t)) + D_{ijkl}(t) \varepsilon_{kl}(\check{\mathbf{u}}) + \int_0^t D_{ijkl}(t-s) \varepsilon_{kl}(\mathbf{w}(s)) ds \quad (21)$$

Using the same Prony series relaxation function as earlier in (16) and substituting in (13) we therefore get,

$$\varrho \dot{\mathbf{w}} - \nabla \cdot \left(\mathbf{C} \boldsymbol{\varepsilon}(\mathbf{w}(t)) + \int_0^t \varphi(t-s) \mathbf{D} \boldsymbol{\varepsilon}(\mathbf{w}(s)) ds \right) = \mathbf{f}(t) + \varphi(t) \mathbf{D} \boldsymbol{\varepsilon}(\check{\mathbf{u}})$$

with $\mathbf{w}(0) = \check{\mathbf{w}}$ given and boundary data for \mathbf{w} derivable from that of \mathbf{u} . This is structurally similar enough to the heat equation (first time derivative, elliptic part in divergence form) that it can be dealt with using the methods described by Werder *et al.* in [43]. The viscoelasticity can be handled either in the form above or through the introduction of internal variables with dynamics described by adjoined ODE's. We will leave further consideration of this model for another time.

3.4 Decoupling in the presence of viscoelastic damping

Now that we have defined the viscoelastic models we introduce them into the DG formulation as given earlier by (3) and obtain the following problem. For each $n = 1, 2, \dots, N$ in turn, find $(U, W, U^1, U^2, \dots, U^{N_\varphi})|_{I_n} \in \mathbb{P}_r(I_n; V) \times \mathbb{P}_r(I_n; V) \times \mathbb{P}_r(I_n; V)^{N_\varphi}$ such that

$$\begin{aligned} & \int_{I_n} (\varrho \dot{W}(t), \vartheta(t)) + a(U(t), \vartheta(t)) + b(\dot{U}(t), \vartheta(t)) dt - \sum_{q=1}^{N_\varphi} \int_{I_n} a(U^q(t), \vartheta(t)) dt \quad (22) \\ & + (\varrho \llbracket W \rrbracket_{n-1}, \vartheta_{n-1}^+) + a(\llbracket U \rrbracket_{n-1}, \zeta_{n-1}^+) + b(\llbracket U \rrbracket_{n-1}, \theta_{n-1}^+) \\ & + \sum_{q=1}^{N_\varphi} \left(\int_{I_n} a(\dot{U}^q(t) + \tau_q^{-1} U^q(t) - \varphi_q U(t), \eta^q(t)) dt + a(\llbracket U^q \rrbracket_{n-1}, \eta_{n-1}^{q+}) \right) \\ & + \int_{I_n} a(\dot{U}(t), \zeta(t)) - a(W(t), \zeta(t)) dt = \int_{I_n} \langle L(t), \vartheta(t) \rangle dt \\ & \forall \vartheta \in \mathbb{P}_r(I_n; V), \quad \forall \{\eta^q\}_{q=1}^{N_\varphi} \subseteq \mathbb{P}_r(I_n; V) \quad \text{and} \quad \forall \zeta \in \mathbb{P}_r(I_n; V). \quad (23) \end{aligned}$$

The decoupling is now a straightforward extension of the method described earlier and by similar means we obtain first,

$$\begin{aligned} & \sum_{j=0}^r \int_{I_n} \left(\dot{\phi}_j(t) \phi_i(t) (\varrho W_j, \vartheta) + \phi_j(t) \phi_i(t) a(U_j, \vartheta) + \dot{\phi}_j(t) \phi_i(t) b(U_j, \vartheta) \right) dt \\ & - \sum_{q=1}^{N_\varphi} \int_{I_n} \phi_j(t) \phi_i(t) dt a(U_j^q, \vartheta) + \sum_{j=0}^r \phi_{j,n-1}^+ \phi_{i,n-1}^+ (\varrho W_j, \vartheta) + \sum_{j=0}^r \phi_{j,n-1}^+ \phi_{i,n-1}^+ b(U_j, \vartheta) \\ & = \int_{I_n} \phi_i(t) \langle L(t), \vartheta \rangle dt + \phi_{i,n-1}^+ (\varrho W_{n-1}^-, \vartheta) + \phi_{i,n-1}^+ b(U_{n-1}^-, \vartheta) \end{aligned}$$

second,

$$\begin{aligned} & \sum_{j=0}^r \int_{I_n} \left(\dot{\phi}_j(t) \phi_i(t) a(U_j, \vartheta) - \phi_j(t) \phi_i(t) a(W_j, \vartheta) \right) dt \\ & + \sum_{j=0}^r \phi_{j,n-1}^+ \phi_{i,n-1}^+ a(U_j, \vartheta) = \phi_{i,n-1}^+ a(U_{n-1}^-, \vartheta), \end{aligned}$$

and third,

$$\begin{aligned} & \sum_{q=1}^{N_\varphi} \sum_{j=0}^r \left(\int_{I_n} \left(\dot{\phi}_j(t) \phi_i(t) a(U_j^q, \eta^q) + \phi_j(t) \phi_i(t) a(\tau_q^{-1} U_j^q - \varphi_q U_j, \eta^q) \right) dt \right. \\ & \left. + \phi_{j,n-1}^+ \phi_{i,n-1}^+ a(U_j^q, \eta^q) - \phi_{i,n-1}^+ a((U^q)_{n-1}^-, \eta^q) \right) = 0. \end{aligned}$$

In our earlier notation these are simply

$$\begin{aligned} & \mathbf{A}_{ij}(\varrho W_j, \vartheta) + \mathbf{M}_{ij} a(U_j, \vartheta) + \mathbf{A}_{ij} b(U_j, \vartheta) - \sum_{q=1}^{N_\varphi} \mathbf{M}_{ij} a(U_j^q, \vartheta) = \mathbf{F}_i(\vartheta), \\ & \mathbf{A}_{ij} a(U_j, \vartheta) - \mathbf{M}_{ij} a(W_j, \vartheta) = \mathbf{G}_i(\vartheta), \\ & \mathbf{A}_{ij} a(U_j^q, \eta^q) + \tau_q^{-1} \mathbf{M}_{ij} a(U_j^q, \eta^q) - \varphi_q \mathbf{M}_{ij} a(U_j, \eta^q) = \mathbf{G}_i^q(\vartheta) \quad \text{for each } q, \end{aligned}$$

and with easily derivable right hand side functionals \mathbf{F} , \mathbf{G} , $\mathbf{G}^1, \dots, \mathbf{G}^{N_\varphi}$. The decoupling is now carried out exactly as before.

4 Numerical experiments

In this section we give a selection of results from some computational experiments. Our main goal is to illustrate the estimated convergence rates, for the standard norms, that are achieved by this scheme. In Subsection 4.1 we focus on the scalar wave equation as described earlier in Subsection 3.1. Then in Subsection 4.2 we give some similar results the viscoelasticity problem with the scheme described earlier in Subsection 3.4. As a practical matter we remark that the enforcement of initial data was, in all cases, done by interpolation rather than projection. Also, except for the Gauss-Lobatto rules used to build the system

matrices for the SEM, all other integrals were computed by using Gauss-Legendre rules of high-enough order to render the contribution of the ‘variational crime’ negligible as compared to the errors that we are interested in. To detail this recall that the Gauss-Legendre n point rule is exact for polynomial integrands of degree $2n - 1$, and we ask that this quadrature rule be exact for the maximum degree that occurs, plus three. This means that for an approximation based on polynomials of degree d we require $2n - 1 = 2d + 3$ and so $n = d + 2$. This is the order of rule used (in space and time — whenever necessary) in our 2D results.

4.1 The acoustic wave equation

We consider several examples, focussing first on a one-space dimensional problem in order to best reveal the (computed) temporal convergence rates. Specifically, for examples 1, 2, 3 and 4 that now follow, we consider a problem that involves different combinations of the Kelvin-Voigt and Maxwell-Zener damping. The problem, with x -dependence suppressed, is

$$\rho \ddot{u}(t) - E_0 u_{xx}(t) - E_1 \dot{u}_{xx}(t) = f(t) - E_0 \int_0^t \varphi_s(t-s) u_{xx}(s) ds \quad \text{in } \Omega \times I, \quad (24)$$

where $\Omega = (0, 1)$ with $T = \pi$ and all data chosen so that $u = x(x-1)\cos(t)$ is the exact solution. Homogeneous Dirichlet boundary data are imposed at each end of Ω and we use both Galerkin and spectral spatial discretization. In these computations we used twelve point Gauss-Legendre integration to compute the spatial inner products ‘exactly’ (except for the SEM system matrices) and for the Galerkin spatial approximation we used a two equal-element mesh for Ω and piecewise quadratics. For the SEM we also used a two element mesh but with piecewise quartics so that the temporal convergence rates would not get smeared by the inexact computation of $L_2(\Omega)$ inner products in the mass matrix.

For the DG time discretization we use piecewise polynomials of degree 1 through 7 and also compute using a Crank-Nicolson (CN), or trapezoidal, discretization of (19) and (20) to give a comparison with a standard and well known scheme. In that ‘CN method’ we put $\mathbf{w} = \dot{\mathbf{u}}$ and then use central differences across a time step for the time derivatives and time nodal-averages for the remaining terms (this is a very standard discretization, see [39] for a similar approach).

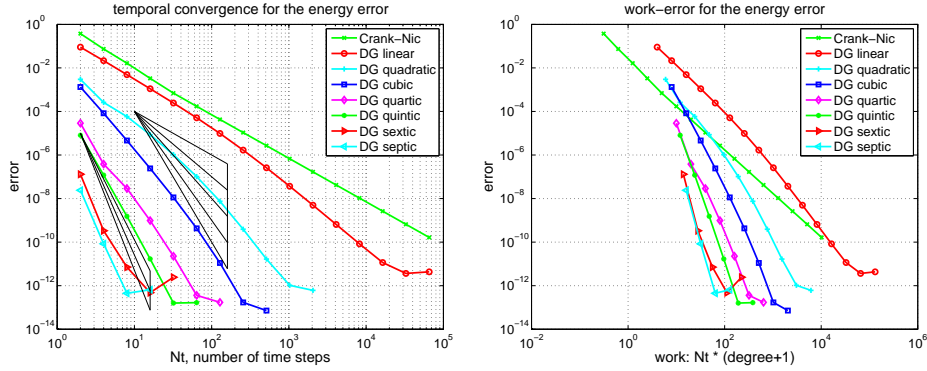
We show only a small selection of the computed results here. The full set are available in the extended report [34].

Example 1 (time error; undamped) *In (24) we choose the density as $\rho = 1010 \text{ Kg/m}^3$, the stiffness modulus as $E_0 = 58 \text{ kPa}$, damping modulus as $E_1 = 0 \text{ Pa} \cdot \text{s}$ and $\varphi(t) = 0$. To save space the results are not shown because they are very similar to those in Example 4 below.*

Example 2 (time error; Kelvin-Voigt) *This is exactly as above for Example 1 but with $E_1 = 30 \text{ kPa} \cdot \text{s}$. The results for the computed energy error bound given by (4) are shown in Figure 1 for the Galerkin error. The spectral element method gave a similar picture.*

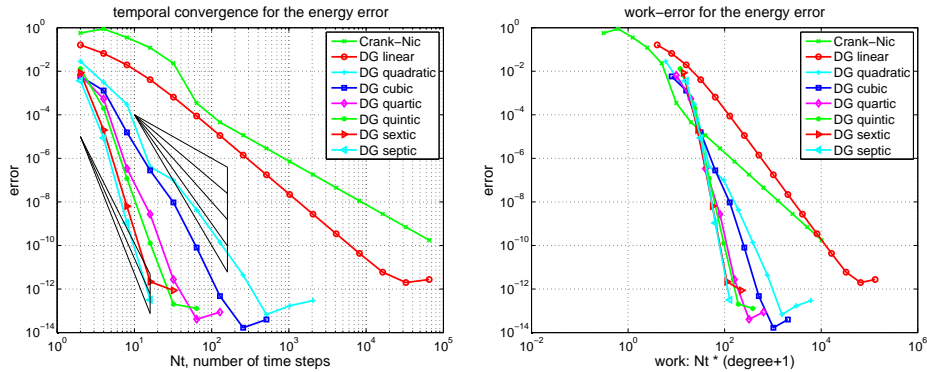
Example 3 (time error; Kelvin-Voigt and Maxwell-Zener) *Similar to Example 2 but with $\varphi(t) = (1 + e^{-t/0.05})/2$. The results are not shown because they are very similar to those in Example 2 above.*

Figure 1: Results for the Example 2 version of (24) showing (left) the energy error, (4), and (right) the corresponding work-error dependence for the Galerkin method.



Example 4 (time error; Maxwell-Zener) Again, similar to Example 2 but with $E_1 = 0$, and $\varphi(t) = (1 + e^{-t/0.05})/2$. The results for the computed energy error bound given by (4) are shown in Figure 2 for the Galerkin error. The spectral element method gave a similar picture.

Figure 2: Results for the Example 4 version of (24) showing (left) the energy error, (4), and (right) the corresponding work-error dependence for the Galerkin method.



In each case the figures show the variation of error with a succession of doublings of time steps ($N = 2, 4, 8, \dots$) and also the variation of error with a measure of the amount of computational work (see below). In the convergence plots we see two ‘fanned triangles’. These indicate the slopes that correspond to error bounds of size $O(k^p)$ for $p \in \{2, 3, 4, 5, 6\}$, for the fan on the right, and $p \in \{7, 8, 9\}$, for the fan on the left.

For the work-error plots we define work as the product of the number of time steps with the number of matrix solves required per time step. For the decoupled DG approximation using polynomials of degree r this latter quantity is of course $r + 1$. For comparison purposes we also show the performance of the Crank-Nicolson method, recalling that it requires only one real-arithmetic solve per time step. Assuming that real-arithmetic multiplications are four times faster than complex, that real-arithmetic additions are twice as fast as complex, and that banded-matrix (of dimension, D , say) inversion is of quadratic complexity with an equal mix of products and sums, we can estimate the operation count of a real inversion as $(D/2)^2 + (D/4)^2 = 5D^2/16$ and that of a complex inversion as $2D^2$. The complex inversion

is therefore around $32/5 = 6.4$ times more expensive. In producing the work-error data for the figures we took one complex inversion as the basic work unit (per time step) and applied the scaling of $5/32$ to the Crank-Nicolson figures to make the comparison fairer. Actual raw wall-clock timings from the example 1 run produced real scalings of around $1/6$ to $1/6.5$ so our approach appears to be well-founded. Of course for larger and more realistic problems an iterative solver will almost certainly be required and the work comparison becomes a much more delicate issue.

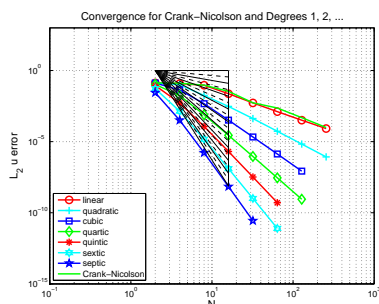
We turn now to problems in two space dimensions and an illustration of space-time error behaviour. The physical data are based on the ‘real life’ problem that we discuss later in Section 5, and the spatial domain is a scaled-up version of the one that we later describe.

For this 2D calculation we chose the domain $\Omega = \{0.005 < x < 0.15 \text{ and } 0 < y < 0.3\}$ with $T = 2$ and the problem $\rho \ddot{u} - G \nabla^2 u = f$ with $\rho = 1010 \text{ kg/m}^3$ and $G = 58 \text{ kPa}$. We took N uniform time steps and, to demonstrate the computed space-time convergence rate, we meshed the domain with an N by N grid. These numerical results use DG-in-time with piecewise polynomials in space and time of degree up to 7, with the same degree being used in both space and time except when indicated. The Crank-Nicolson (CN) computations are based on piecewise linears for the spatial approximations, with quadratics being used in the bottom row of the figures—as explained more fully in the first example. In the convergence graphs that follow, the triangle fans indicate convergence rates from zero to nine in half-steps.

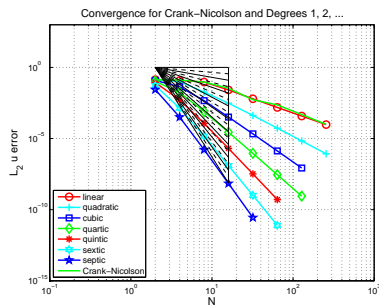
Example 5 (space-time error for the wave equation, Dirichlet BC’s) *Here Dirichlet boundary data are assumed on the whole of $\partial\Omega$, and f , the boundary and the initial data are chosen so that the exact solution is $u = \cos(2\pi t) \sin(40\pi x) \cos(30\pi y)$. The results are plotted on the left of the top row in Figures 3, 4 and 5 for the Galerkin-in-space scheme for errors in $u(T)$, $\nabla u(T)$ and $w(T)$, with the estimated convergence rates tabulated on the right. (Notice that a zero value of L_2 error for w is reported for the CN scheme when $N = 2$ — this is no more than a numerical anomaly resulting from exact boundary data and a very coarse mesh.) These are based on the computed errors for N (first column) and for $2N$ (the results for $N = 4$ use those for $N = 2$, the row for which is not shown). The middle row of the figure shows the result of computing with one degree higher polynomials in time than in space, while the bottom row shows the result of using one degree higher in space than in time. The CN results are of course unaffected in the middle row. Figures 6, 7 and 8 show analogous results for the spectral element scheme in the case where equal degrees are used.*

Example 6 (space-time error for the wave equation, Mixed BC’s) *This example is set-up exactly as for Example 5 except that homogeneous (because at $r = 0.15$ we have $\sin(40\pi r) = 0$) Dirichlet boundary data are imposed on the right-hand edge of the domain, with Neumann data everywhere else on $\partial\Omega$. The results are plotted on the left of the top row in Figures 9, 10 and 11 for the Galerkin-in-space scheme for errors in $u(T)$, $\nabla u(T)$ and $w(T)$, with the estimated convergence rates tabulated on the right. These are based on the computed errors for N (first column) and for $2N$ (the results for $N = 4$ use those for $N = 2$, the row for which is not shown). The middle row of the figure shows the result of computing with one degree higher polynomials in time than in space, while the bottom row shows the result of using one degree higher in space than in time. The CN results are of course unaffected in the middle row. Figures 12, 13 and 14 show analogous results for the spectral element scheme in the case where equal degrees are used.*

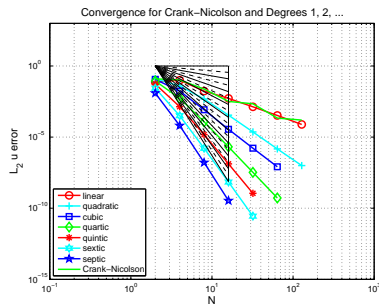
Figure 3: Plots of the $L_2(\Omega)$ error in $u(T)$ against N (equal in space and time) for the wave equation problem in Example 5 (Galerkin-in-space).



N	CN	1	2	3	4	5	6	7
4	0.07	0.15	0.44	1.60	2.60	4.09	5.25	6.44
8	0.48	0.38	2.51	3.22	4.47	5.46	6.54	7.59
16	1.44	1.98	2.55	3.84	4.81	5.85	6.87	7.89
32	2.68	2.15	2.84	3.93	4.95	5.96	6.97	7.97
64	1.22	2.04	2.97	3.98	4.99	5.99	6.99	—
128	2.25	2.00	2.99	4.00	5.00	—	—	—
256	2.29	1.96	3.00	—	—	—	—	—

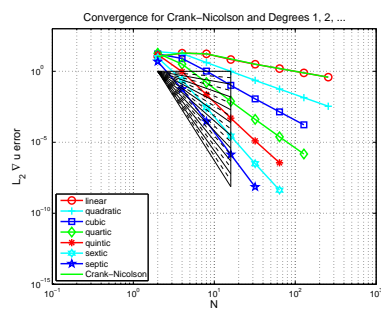


N	CN	1	2	3	4	5	6	7
4	0.07	0.20	0.48	1.48	2.62	4.08	5.25	6.44
8	0.48	0.38	2.42	3.23	4.46	5.46	6.54	7.59
16	1.44	1.84	2.61	3.84	4.81	5.85	6.87	7.89
32	2.68	2.07	2.85	3.93	4.95	5.96	6.97	7.97
64	1.22	2.02	2.97	3.98	4.99	5.99	6.99	—
128	2.25	2.00	2.99	3.99	5.00	—	—	—
256	2.29	2.00	3.00	—	—	—	—	—

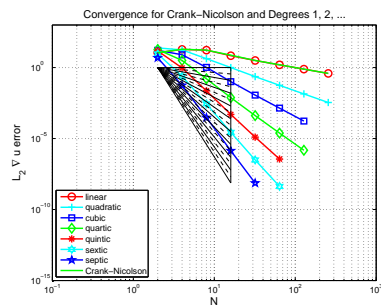


N	CN	1	2	3	4	5	6	7
4	0.27	-0.44	1.74	2.73	4.05	5.29	6.44	7.58
8	2.12	2.54	3.03	4.37	5.48	6.53	7.59	8.63
16	2.88	1.71	3.78	4.55	5.85	6.83	7.89	8.90
32	0.56	1.96	3.92	4.42	5.96	6.87	7.97	—
64	3.34	2.02	3.96	4.34	5.98	—	—	—
128	0.46	2.09	3.90	—	—	—	—	—

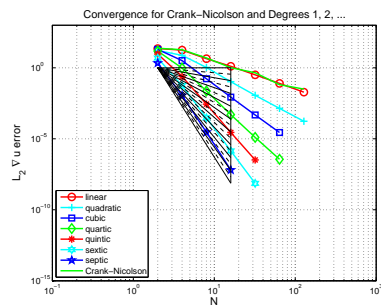
Figure 4: Plots of the $L_2(\Omega)$ error in $\nabla u(T)$ against N (equal in space and time) for the wave equation problem in Example 5 (Galerkin-in-space).



N	CN	1	2	3	4	5	6	7
4	-0.81	-0.79	0.44	1.06	2.54	4.02	5.22	6.44
8	0.21	0.16	2.09	2.95	4.32	5.33	6.48	7.54
16	1.17	1.33	2.07	3.34	4.39	5.53	6.65	7.75
32	1.24	1.11	2.11	3.16	4.23	5.32	6.45	7.58
64	1.01	1.02	2.04	3.05	4.08	5.12	6.19	-
128	1.02	1.00	2.01	3.01	4.02	-	-	-
256	1.01	1.00	2.00	-	-	-	-	-



N	CN	1	2	3	4	5	6	7
4	-0.81	-0.76	0.46	1.04	2.55	4.01	5.21	6.44
8	0.21	0.17	2.05	2.95	4.31	5.33	6.48	7.54
16	1.17	1.30	2.09	3.33	4.39	5.53	6.65	7.75
32	1.24	1.12	2.11	3.16	4.23	5.32	6.45	7.58
64	1.01	1.02	2.05	3.05	4.08	5.12	6.19	-
128	1.02	1.01	2.01	3.01	4.02	-	-	-
256	1.01	1.00	2.00	-	-	-	-	-



N	CN	1	2	3	4	5	6	7
4	0.35	0.36	1.14	2.63	3.98	5.25	6.44	7.57
8	1.92	2.01	2.83	4.25	5.35	6.47	7.54	8.61
16	2.28	1.79	3.34	4.30	5.54	6.63	7.75	8.82
32	1.18	1.98	3.18	4.17	5.32	6.44	7.58	-
64	2.79	2.01	3.06	4.11	5.12	-	-	-
128	1.04	2.05	3.02	-	-	-	-	-

Figure 5: Plots of the $L_2(\Omega)$ error in $w(T)$ against N (equal in space and time) for the wave equation problem in Example 5 (Galerkin-in-space).

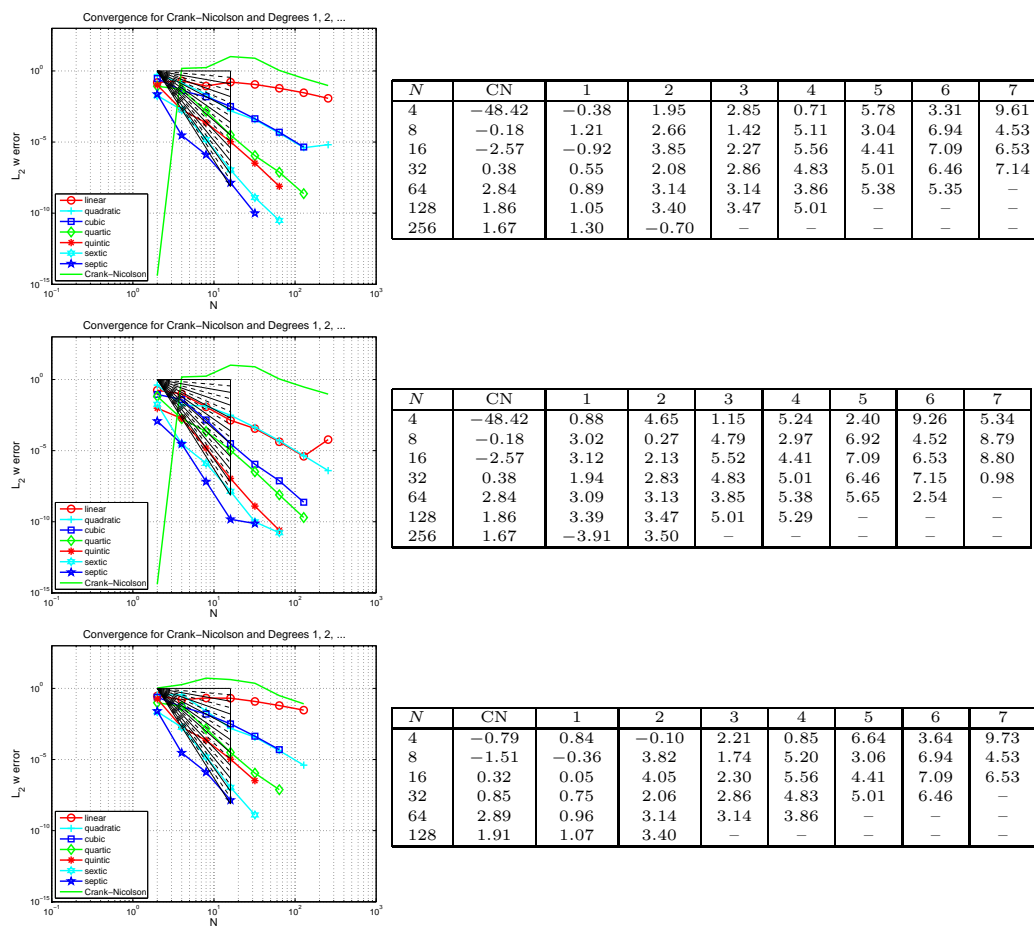


Figure 6: Plots of the $L_2(\Omega)$ error in $u(T)$ against N (equal in space and time) for the wave equation problem in Example 5 (spectral-element-in-space).

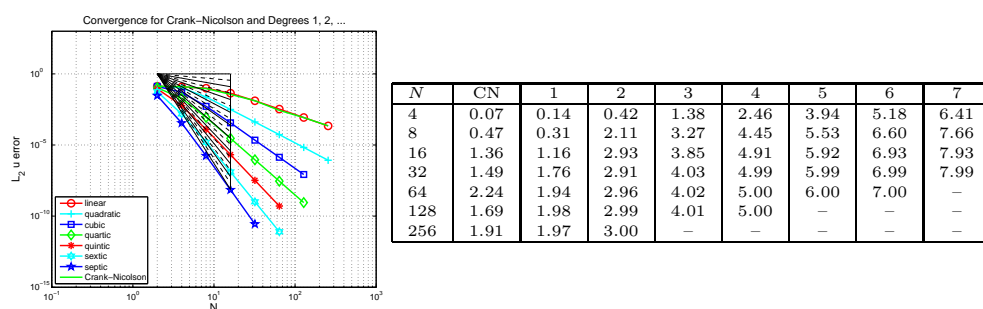


Figure 7: Plots of the $L_2(\Omega)$ error in $\nabla u(T)$ against N (equal in space and time) for the wave equation problem in Example 5 (spectral-element-in-space).

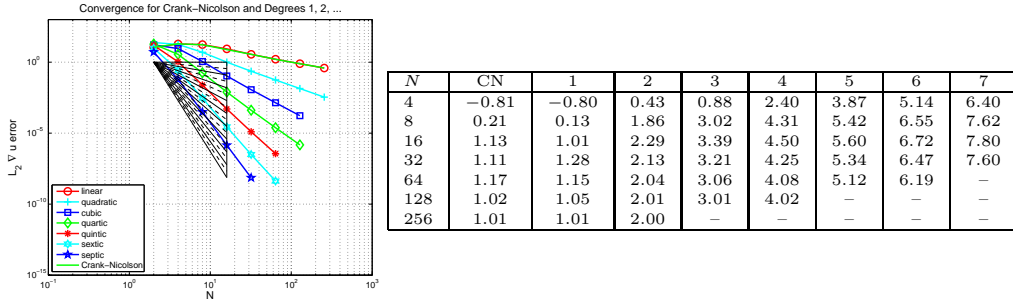
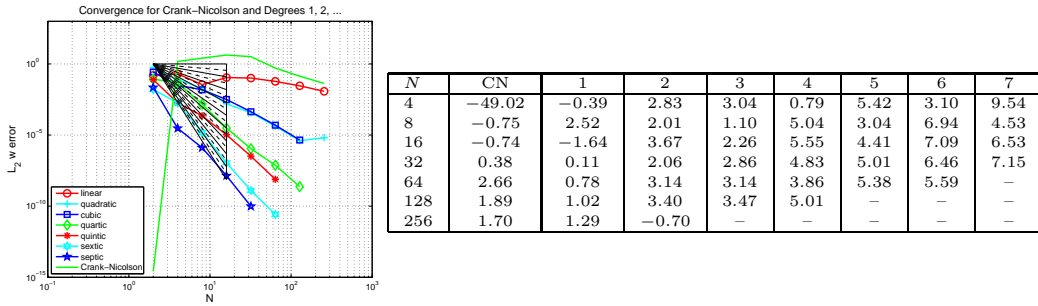


Figure 8: Plots of the $L_2(\Omega)$ error in $w(T)$ against N (equal in space and time) for the wave equation problem in Example 5 (spectral-element-in-space).



4.2 Elasto- and Visco-dynamics

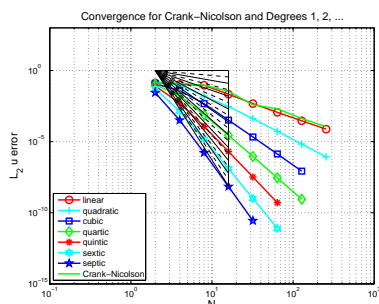
In this subsection we give a numerical demonstration of this scheme for the elasticity and viscoelasticity problems described earlier in Subsection 3.2 except that, due to the considerations in Subsection 3.3, we set $\mathbf{C} = \mathbf{Q}$ in (14). Also, unless stated otherwise, the set-up for the numerical results is exactly as for the wave equation as described in the previous section.

Example 7 (space-time error for viscodynamics, Mixed BC's) For this 2D calculation we choose the same domain as above, $\Omega = \{0.005 < x < 0.15 \text{ and } 0 < y < 0.3\}$ but now with $T = 0.5$ and the problem given by (19) and (20). We set $\rho = 1010 \text{ kg/m}^3$, $E = 167 \text{ kPa}$, Poisson's ratio $\nu = 0.44$ and include viscoelastic effects by choosing $\varphi_0 = 0.2$, $\varphi_1 = 0.8$ and $\tau_1 = 0.05$ in (16). The load, f , boundary and initial data are chosen so that the exact solution is $(u_1, u_2)^T = (\sin(2\pi x) \sin(2\pi y) \cos(2\pi t + \pi/4), \cos(2\pi x) \sin(2\pi y) \sin(2\pi t - \pi/4))^T$ and Dirichlet data were prescribed on bottom edge of $\partial\Omega$ with tractions prescribed elsewhere. The results are given in Figures 15, 16 and 17 for the Galerkin-in-space scheme and in Figures 18, 19 and 20 for the spectral element scheme. These results are for the case where equal polynomial degrees in space and time were used.

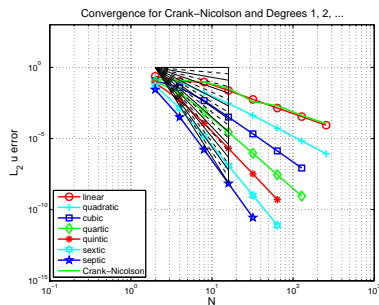
5 Application: shear waves in biotissue-mimicking gel

In this section we shift our focus away from exact errors and manufactured solutions to a much more practical experimental set-up. We consider an annular cylinder of tissue mim-

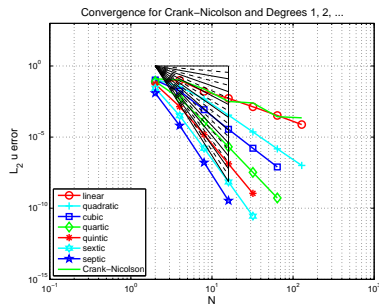
Figure 9: Plots of the $L_2(\Omega)$ error in $u(T)$ against N (equal in space and time) for the wave equation problem in Example 6 (Galerkin-in-space).



N	CN	1	2	3	4	5	6	7
4	0.07	0.35	0.71	1.58	2.56	4.01	5.23	6.42
8	0.47	0.18	2.65	3.07	4.47	5.45	6.54	7.59
16	1.46	2.11	2.40	3.84	4.80	5.85	6.88	7.89
32	3.13	2.17	2.82	3.93	4.95	5.96	6.97	7.97
64	0.93	2.04	2.96	3.98	4.99	5.99	6.99	—
128	2.27	1.99	2.99	4.00	5.00	—	—	—
256	1.92	1.94	3.00	—	—	—	—	—

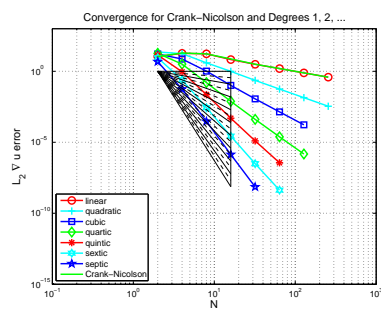


N	CN	1	2	3	4	5	6	7
4	0.07	1.19	0.74	1.55	2.57	3.99	5.23	6.42
8	0.47	0.17	2.57	3.08	4.45	5.45	6.54	7.59
16	1.46	1.96	2.47	3.83	4.80	5.85	6.88	7.89
32	3.13	2.08	2.83	3.93	4.95	5.96	6.97	7.97
64	0.93	2.02	2.97	3.98	4.99	5.99	6.99	—
128	2.27	2.00	2.99	3.99	5.00	—	—	—
256	1.92	2.00	3.00	—	—	—	—	—

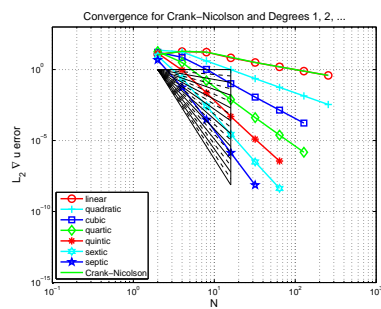


N	CN	1	2	3	4	5	6	7
4	0.27	-0.41	1.74	2.58	3.96	5.27	6.42	7.58
8	2.12	2.60	2.86	4.36	5.47	6.53	7.59	8.63
16	2.90	1.61	3.78	4.56	5.85	6.84	7.89	8.90
32	0.35	1.97	3.91	4.43	5.96	6.88	7.97	—
64	3.21	2.03	3.95	4.38	5.98	—	—	—
128	0.27	2.11	3.88	—	—	—	—	—

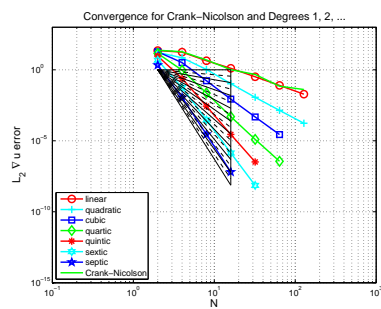
Figure 10: Plots of the $L_2(\Omega)$ error in $\nabla u(T)$ against N (equal in space and time) for the wave equation problem in Example 6 (Galerkin-in-space).



N	CN	1	2	3	4	5	6	7
4	-0.81	-0.75	0.40	1.19	2.51	3.96	5.20	6.42
8	0.21	0.12	2.15	2.82	4.32	5.31	6.48	7.54
16	1.18	1.35	2.00	3.34	4.39	5.53	6.65	7.75
32	1.25	1.10	2.10	3.16	4.22	5.32	6.45	7.58
64	1.01	1.01	2.04	3.05	4.08	5.12	6.19	-
128	1.01	1.00	2.01	3.01	4.02	-	-	-
256	1.01	1.00	2.00	-	-	-	-	-

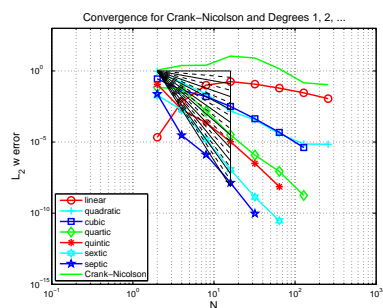


N	CN	1	2	3	4	5	6	7
4	-0.81	-0.62	0.41	1.16	2.53	3.95	5.20	6.43
8	0.21	0.13	2.11	2.83	4.31	5.31	6.48	7.54
16	1.18	1.33	2.02	3.33	4.38	5.53	6.65	7.75
32	1.25	1.10	2.10	3.16	4.22	5.32	6.45	7.58
64	1.01	1.02	2.04	3.05	4.08	5.11	6.19	-
128	1.01	1.00	2.01	3.01	4.02	-	-	-
256	1.01	1.00	2.00	-	-	-	-	-

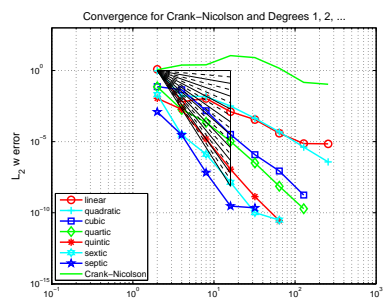


N	CN	1	2	3	4	5	6	7
4	0.35	0.37	1.24	2.54	3.92	5.24	6.42	7.57
8	1.92	2.01	2.73	4.25	5.33	6.47	7.54	8.61
16	2.28	1.77	3.34	4.30	5.54	6.63	7.75	8.82
32	1.11	1.99	3.18	4.17	5.32	6.43	7.58	-
64	2.74	2.02	3.06	4.11	5.12	-	-	-
128	0.78	2.05	3.02	-	-	-	-	-

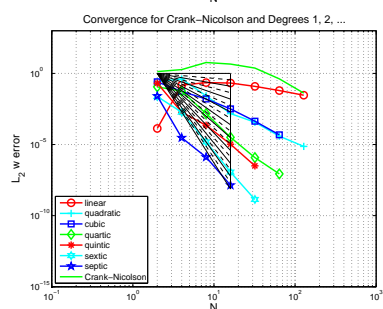
Figure 11: Plots of the $L_2(\Omega)$ error in $w(T)$ against N (equal in space and time) for the wave equation problem in Example 6 (Galerkin-in-space).



N	CN	1	2	3	4	5	6	7
4	-1.09	-8.23	2.63	2.65	0.37	5.95	3.39	9.65
8	-0.05	-3.93	2.61	1.48	5.17	3.05	6.94	4.53
16	-2.15	-0.84	4.04	2.30	5.54	4.43	7.05	6.56
32	0.46	0.59	2.03	2.88	4.75	5.05	6.40	7.18
64	2.50	0.93	3.24	3.18	3.79	5.45	5.55	-
128	3.30	1.09	2.39	3.55	5.62	-	-	-
256	0.44	1.37	0.09	-	-	-	-	-

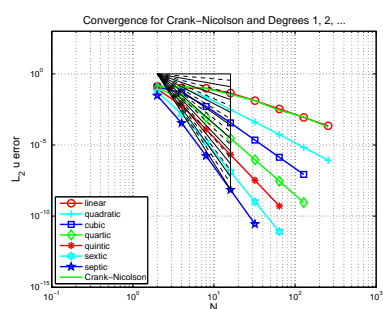


N	CN	1	2	3	4	5	6	7
4	-1.09	7.57	5.86	0.74	5.29	2.56	9.38	5.38
8	-0.05	-0.78	0.17	4.89	3.00	6.93	4.53	8.79
16	-2.15	3.09	2.19	5.53	4.43	7.05	6.56	7.83
32	0.46	1.85	2.87	4.75	5.05	6.40	7.08	0.42
64	2.50	3.19	3.18	3.79	5.45	5.62	1.74	-
128	3.30	2.40	3.55	5.62	5.24	-	-	-
256	0.44	0.08	3.45	-	-	-	-	-



N	CN	1	2	3	4	5	6	7
4	-0.47	-10.12	-0.58	2.25	1.01	6.77	3.66	9.73
8	-1.66	-0.60	3.91	1.76	5.22	3.06	6.94	4.53
16	0.38	0.10	4.15	2.31	5.54	4.43	7.05	6.56
32	0.92	0.78	2.04	2.88	4.75	5.05	6.40	-
64	2.52	0.97	3.24	3.18	3.79	-	-	-
128	3.32	1.10	2.39	-	-	-	-	-

Figure 12: Plots of the $L_2(\Omega)$ error in $u(T)$ against N (equal in space and time) for the wave equation problem in Example 6 (spectral-element-in-space).



N	CN	1	2	3	4	5	6	7
4	0.07	0.35	0.53	1.29	2.43	3.89	5.16	6.40
8	0.47	0.10	2.14	3.23	4.42	5.53	6.60	7.66
16	1.36	1.13	2.92	3.82	4.91	5.92	6.93	7.93
32	1.48	1.77	2.87	4.03	4.99	5.99	6.99	7.99
64	2.23	1.94	2.94	4.02	5.00	6.00	7.00	-
128	1.56	1.98	2.99	4.01	5.00	-	-	-
256	2.38	1.97	3.00	-	-	-	-	-

Figure 13: Plots of the $L_2(\Omega)$ error in $\nabla u(T)$ against N (equal in space and time) for the wave equation problem in Example 6 (spectral-element-in-space).

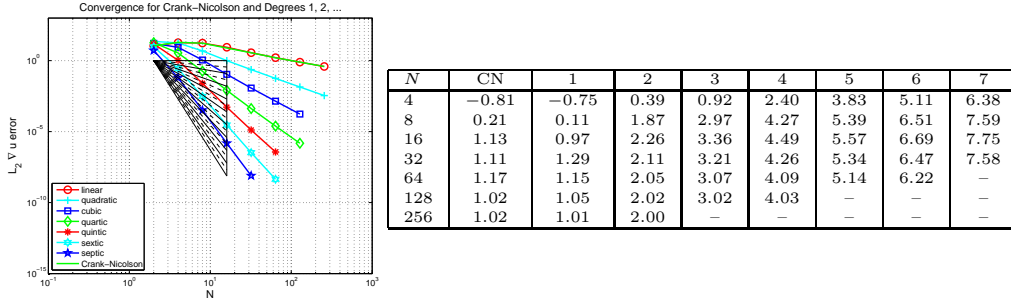


Figure 14: Plots of the $L_2(\Omega)$ error in $w(T)$ against N (equal in space and time) for the wave equation problem in Example 6 (spectral-element-in-space).

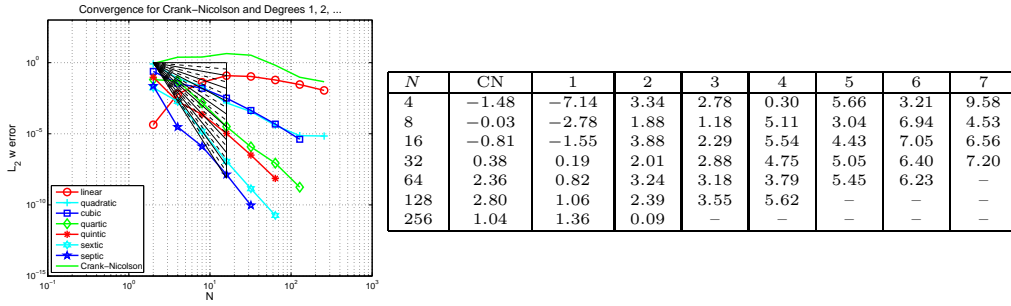


Figure 15: Plots of the $L_2(\Omega)$ error in $u(T)$ against N (equal in space and time) for the viscodynamic problem in Example 7 (Galerkin-in-space).

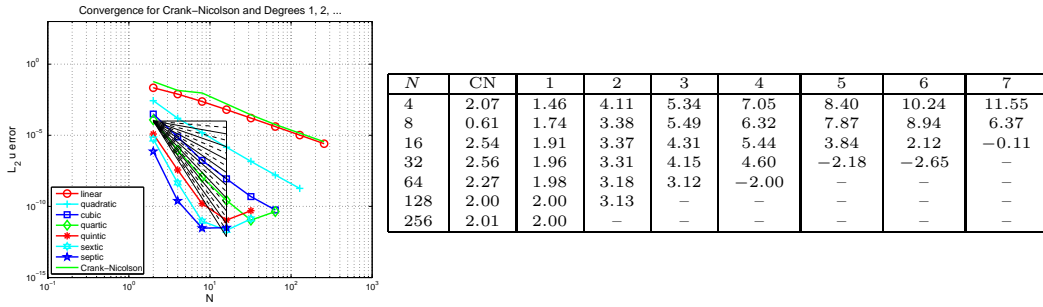


Figure 16: Plots of the $L_2(\Omega)$ error in $\nabla u(T)$ against N (equal in space and time) for the viscodynamic problem in Example 7 (Galerkin-in-space).

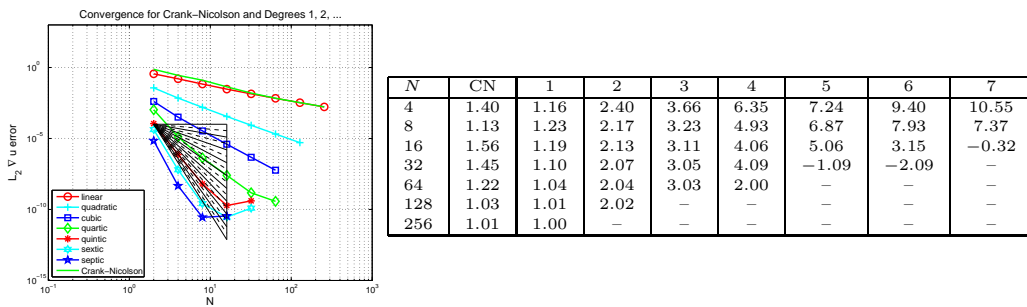


Figure 17: Plots of the $L_2(\Omega)$ error in $w(T)$ against N (equal in space and time) for the viscodynamic problem in Example 7 (Galerkin-in-space).

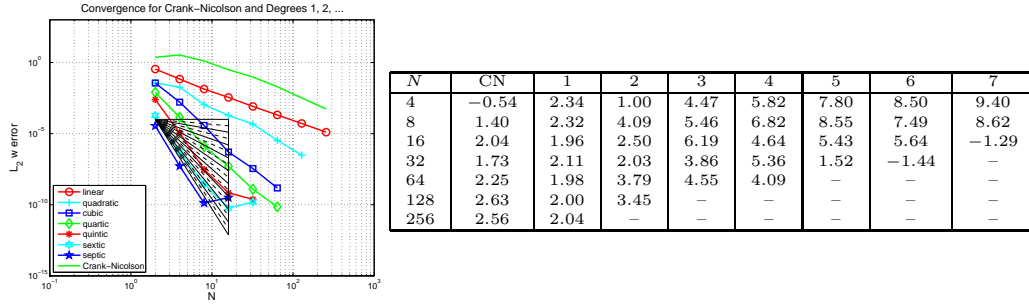


Figure 18: Plots of the $L_2(\Omega)$ error in $u(T)$ against N (equal in space and time) for the viscodynamic problem in Example 7 (spectral-element-in-space).

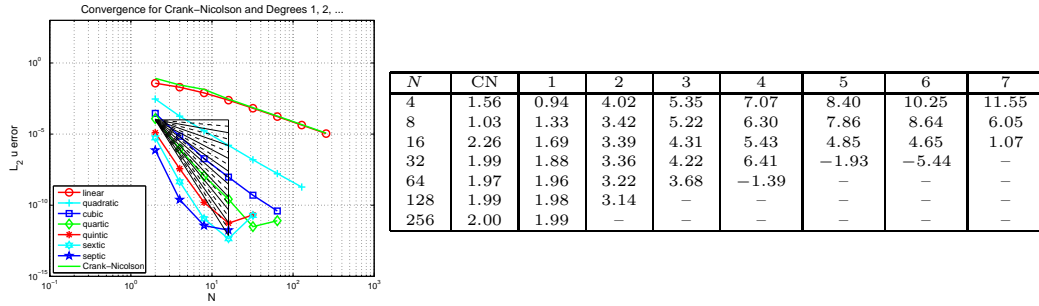


Figure 19: Plots of the $L_2(\Omega)$ error in $\nabla u(T)$ against N (equal in space and time) for the viscodynamic problem in Example 7 (spectral-element-in-space).

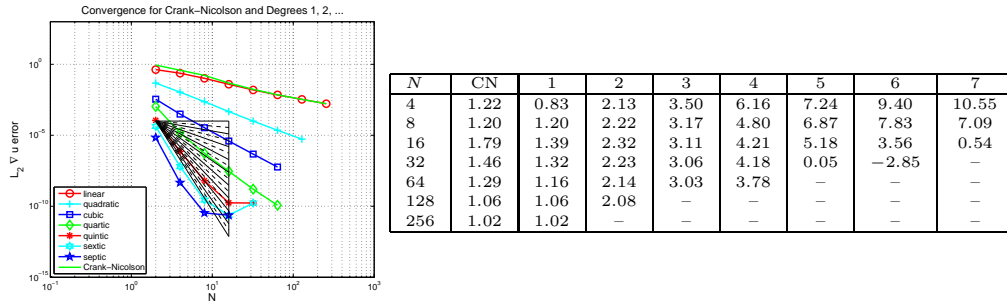


Figure 20: Plots of the $L_2(\Omega)$ error in $w(T)$ against N (equal in space and time) for the viscodynamic problem in Example 7 (spectral-element-in-space).

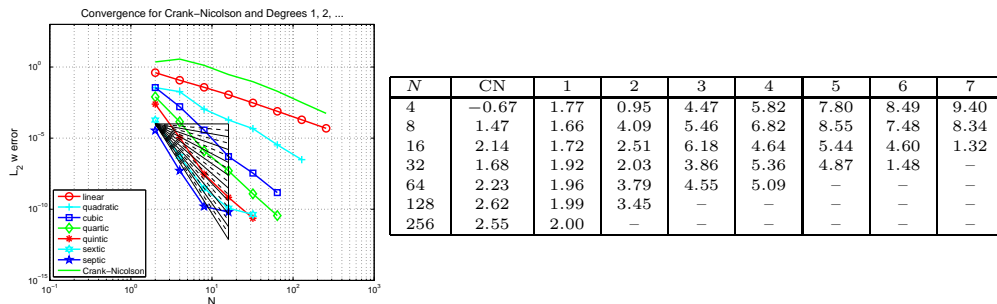
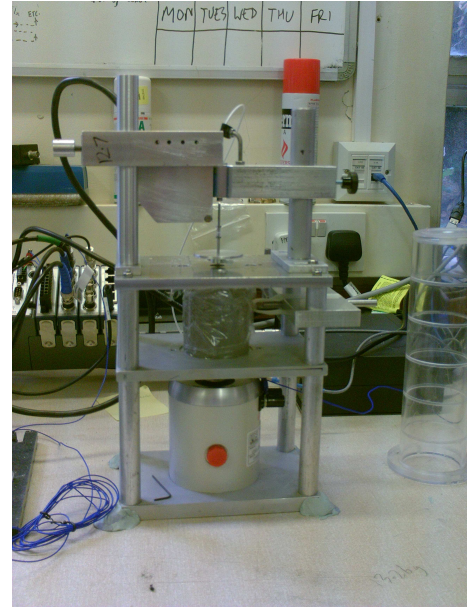
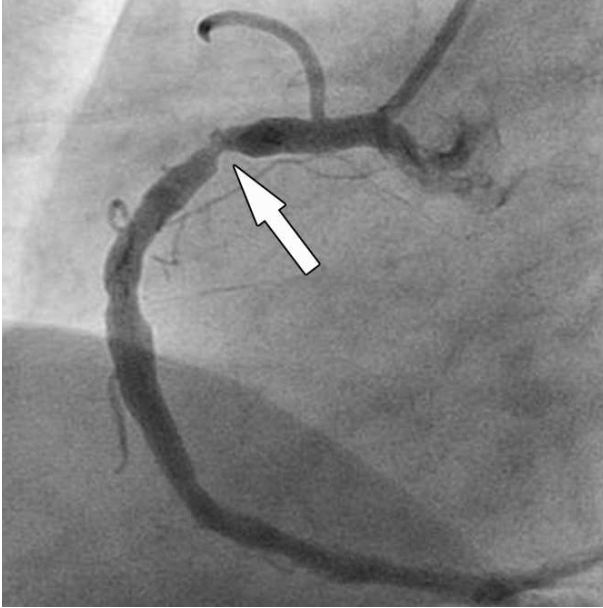


Figure 21: On the left (reproduced by permission from Figure 4b in [9] ©RSNA 2009) an image of a right proximal coronary artery stenosis obtained by X-Ray angiography after injecting a contrast medium through a catheter passed into the aorta and thence into the root of the coronary vessel. On the right an illustration of our experimental rig referred to in Section 5. The middle section of the scaffold contains the gel phantom wrapped in film to prevent dehydration. The rod containing a moulded-in bead is visible emerging from the top and the unit at the bottom is the controllable ‘shaker’ which imparts the bead’s vertically linear vibration. This bead is mimicked in our computational set up by the traction in (25). The displacement of the rod and bead assembly is measured by an optical device at the top of the rig, removed in this picture for clarity.



icking agarose gel of height 0.0514 m and with inner and outer radii 0.00175 m and 0.027 m. Here ‘height’ indicates that the cylinder is up-ended so that the radial plane is horizontal.

This experimental rig actually exists in our laboratories (see the right of Figure 21) and is the first step in an ambitious project investigating the possibility of diagnosing coronary artery disease through computational mathematics. Briefly, plaque build-up in a diseased coronary artery causes a stenosis (see the left of Figure 21) which induces downstream turbulent blood flow. It is hypothesized that the resulting wall shear stress causes a 500 — 1500 Hz acoustic shear wave, or *bruit*, which travels through the thorax and which is audible on the chest wall. Our project has a long term aim to couple an inverse solver algorithm with an efficient forward solver to simulate the passage of these shear waves through viscoelastic soft tissue, produce a signal on the chest surface and, by comparing with a ‘real signal’ from a patient, use the difference in these signals to identify and locate the disease.

We refer to [6, 7, 40] for a much more detailed treatment of the background to both the biomedical science and the proposed methodology and algorithm; to [4] and [5] for full details of the inverse problem; and, to [11] for the experimental protocol and findings.

The small rig referred to above, and in Figure 21, is but the first step towards this long-term objective and it is necessary to develop an efficient forward solver that can at least deal with this experimental set up. Thus, here, we work in cylindrical polar coordinates and restrict

Figure 22: Computed signals for 250 Hz on a 25×50 mesh with (left) 6000 CN and 500 DG(3) and (right) 12000 CN and 750 DG(3) time steps.

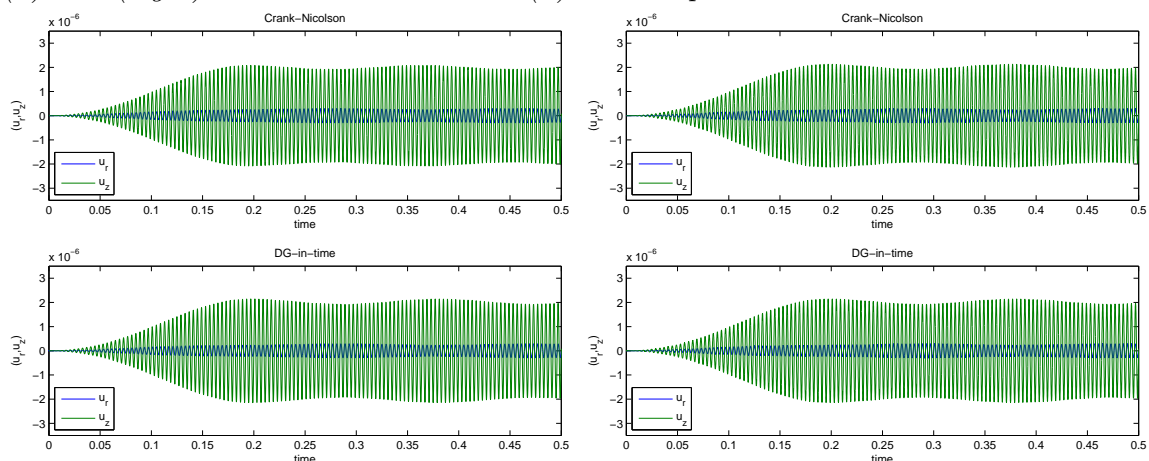


Figure 23: Computed signals for 250 Hz on a 13×25 mesh with (left) 6000 CN and 500 DG(3) and (right) 12000 CN and 750 DG(3) time steps.

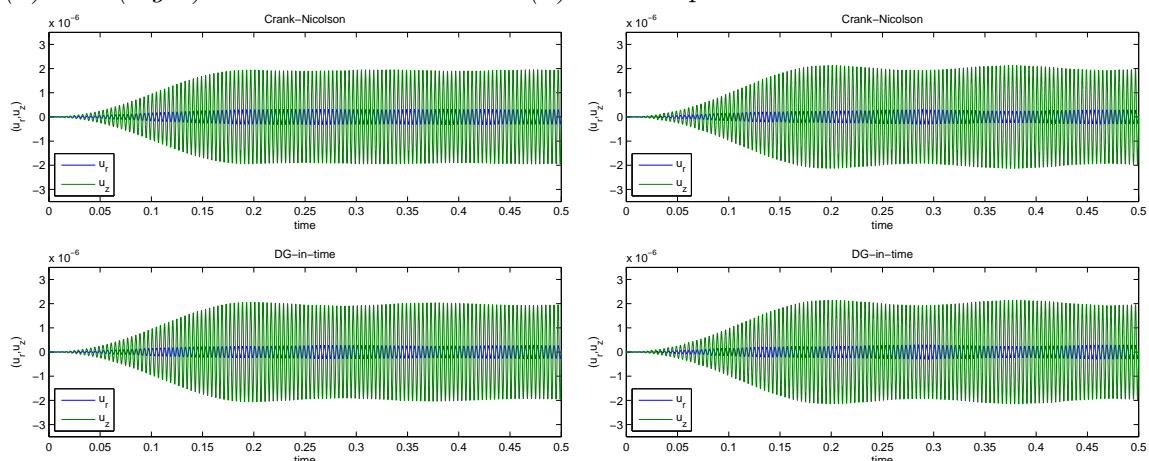


Figure 24: Computed signals for 500 Hz on a 13×25 mesh with (left) 24000 CN and 1500 DG(3) and (right) 48000 CN and 3000 DG(3) time steps.

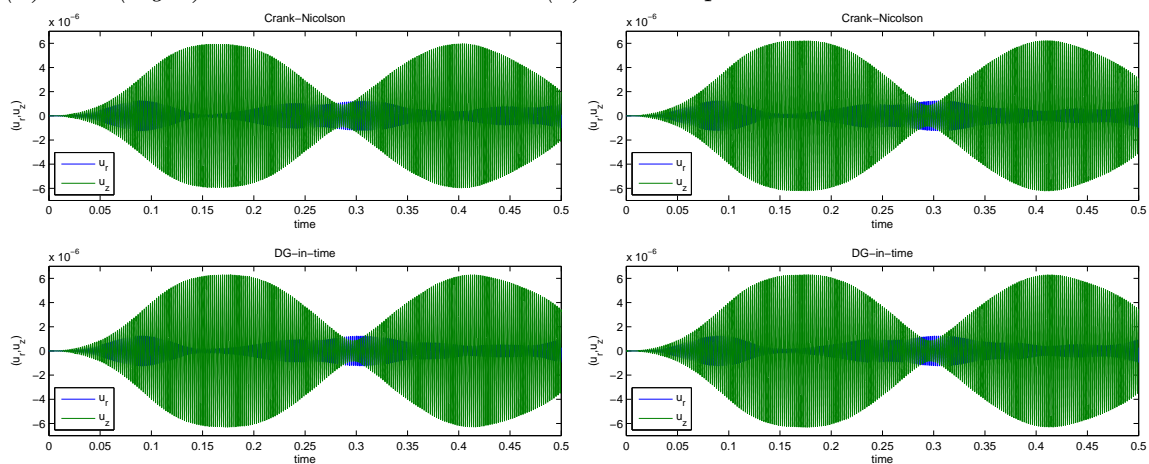


Figure 25: *Computed signals for 750 Hz on a 13×25 mesh with (left) 36000 CN and 2250 DG(3) and (right) 96000 CN and 6000 DG(3) time steps.*

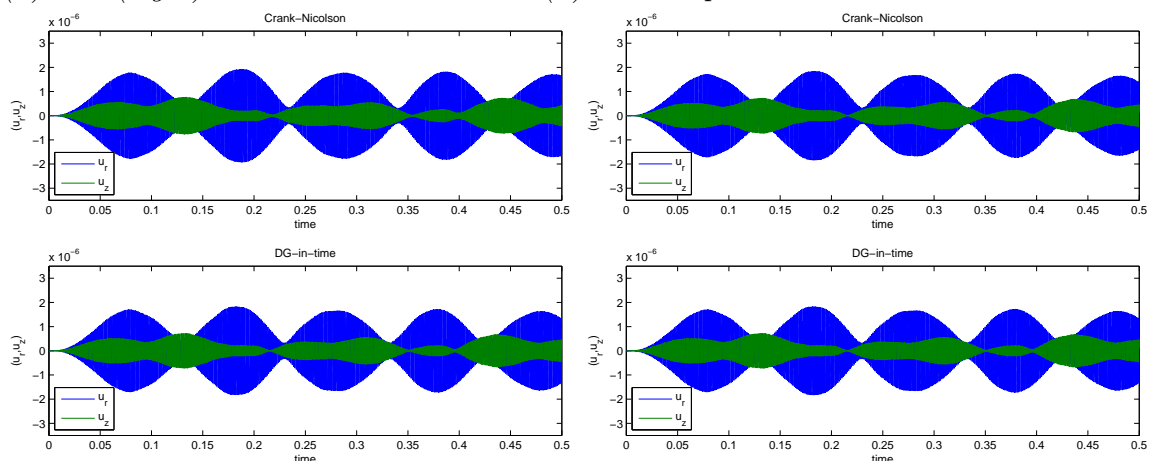


Figure 26: *Computed signals for 1000 Hz on a 13×25 mesh with (left) 48000 CN and 3000 DG(3) and (right) 144000 CN and 9000 DG(3) time steps.*

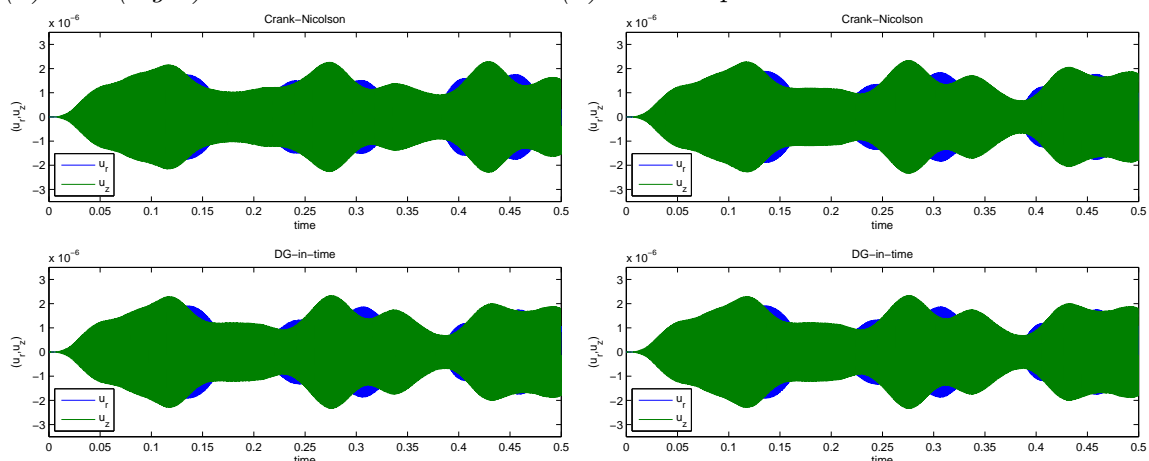


Figure 27: *Computed signals for 1250 Hz on a 13×25 mesh with (left) 48000 CN and 3000 DG(3) and (right) 288000 CN and 18000 DG(3) time steps.*

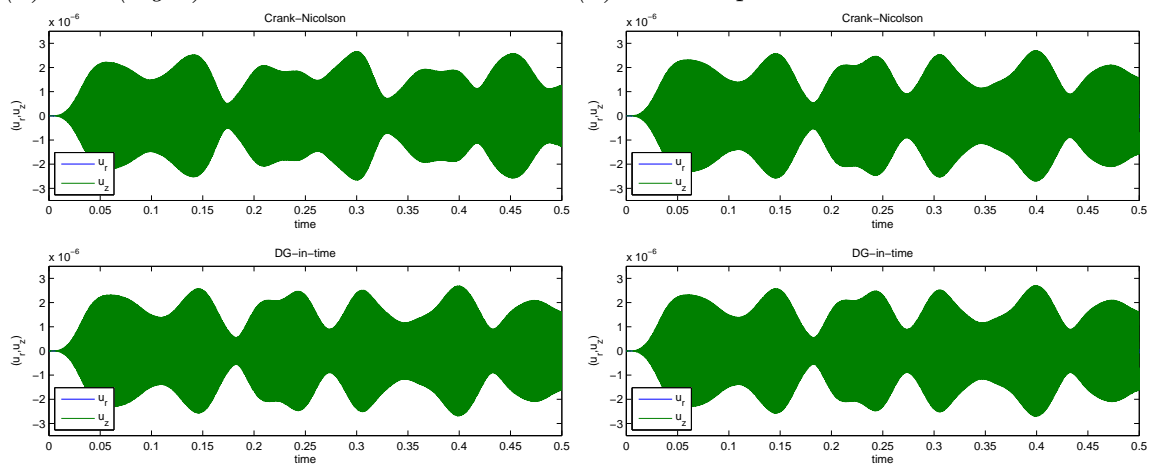


Figure 28: Computed signals for 1250 Hz on a 25×50 mesh with (left) 72000 CN and 4500 DG(3) and (right) 288000 CN and 18000 DG(3) time steps.

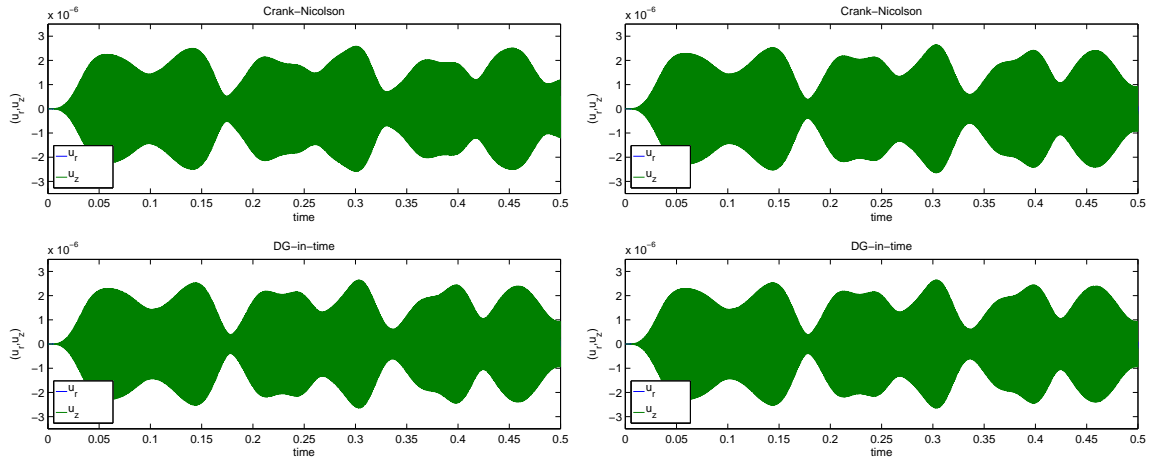


Figure 29: Approximated errors and 'tic-toc' MATLAB $\text{\textcircled{R}}$ timings in minutes for the 250 Hz run with CN and DG(3) on a 25×50 mesh.

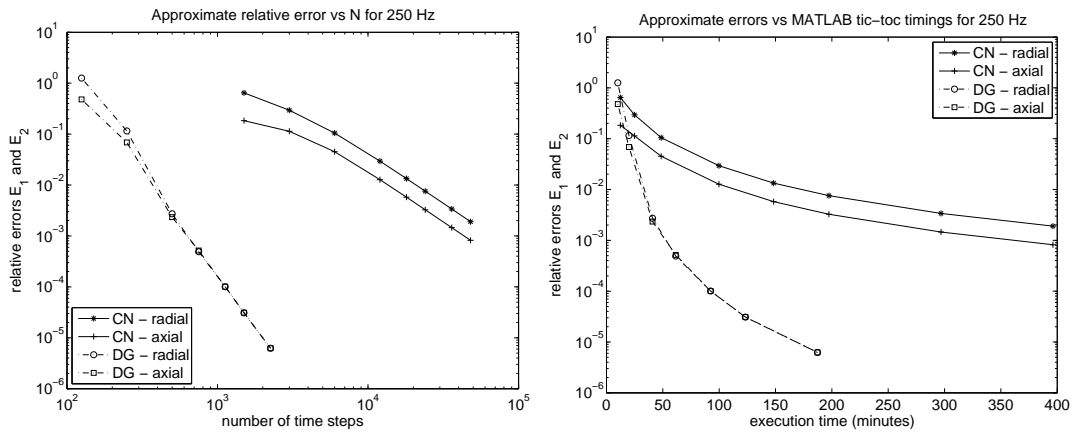


Figure 30: Approximated errors and 'tic-toc' MATLAB $\text{\textcircled{R}}$ timings in minutes for the 250 Hz run with CN and DG(3) on a 13×25 mesh.

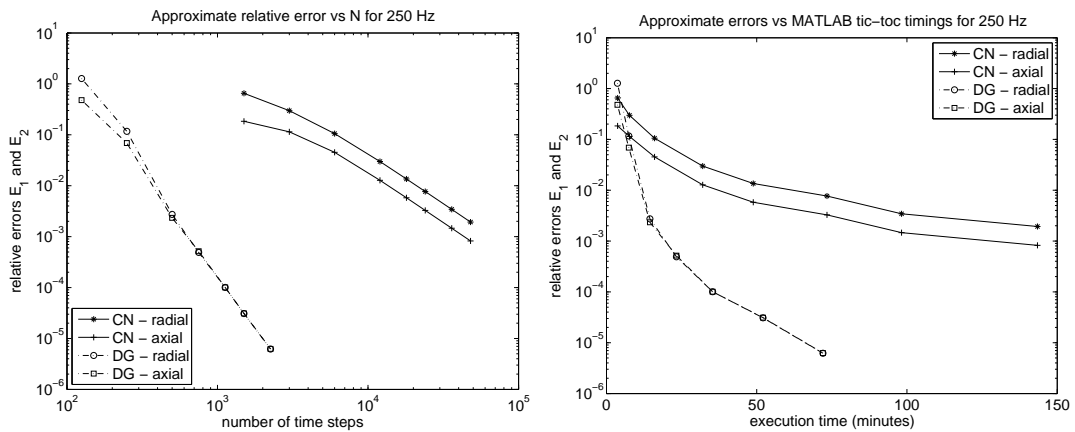


Figure 31: *Approximated errors and 'tic-toc' MATLAB $\text{\textcircled{R}}$ timings in minutes for the 500 Hz run with CN and DG(3) on a 13×25 mesh.*

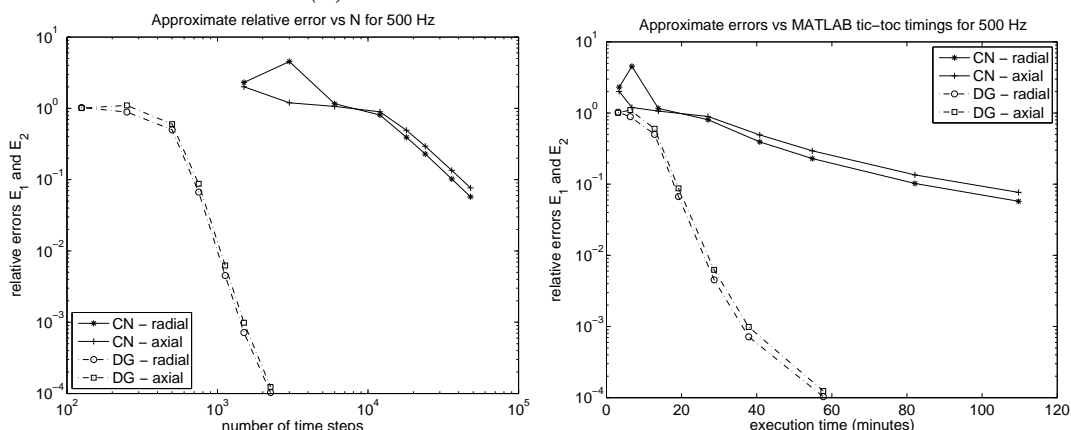


Figure 32: *Approximated errors and 'tic-toc' MATLAB $\text{\textcircled{R}}$ timings in minutes for the 750 Hz run with CN and DG(3) on a 13×25 mesh.*

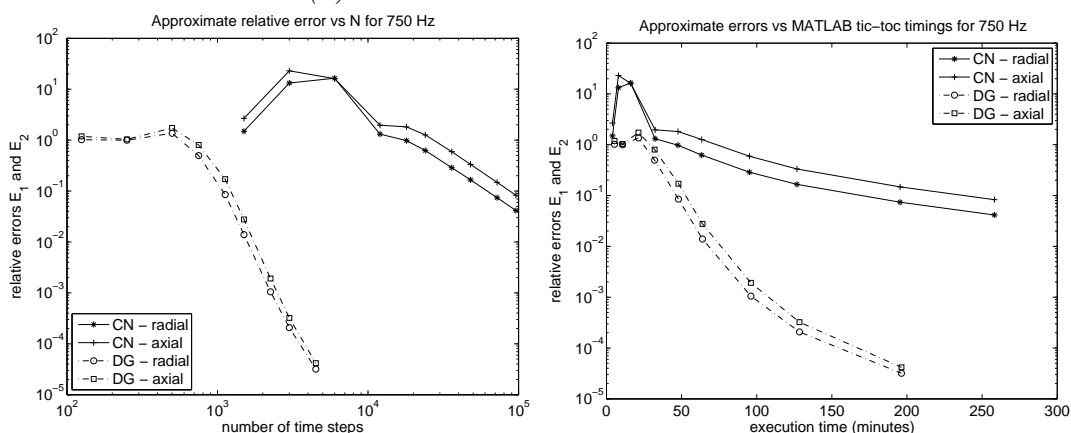


Figure 33: *Approximated errors and 'tic-toc' MATLAB $\text{\textcircled{R}}$ timings in minutes for the 1000 Hz run with CN and DG(3) on a 13×25 mesh.*

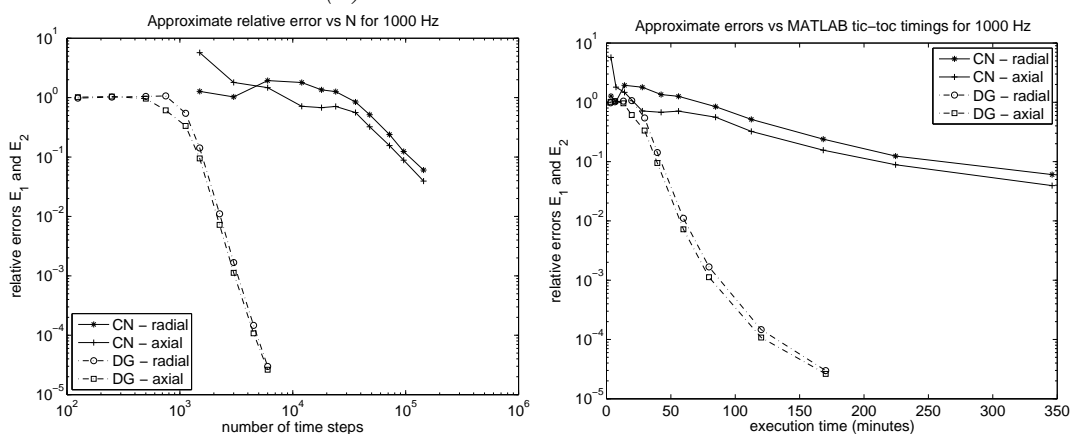


Figure 34: *Approximated errors and 'tic-toc' MATLAB [®] timings in minutes for the 1250 Hz run with CN and DG(3) on a 13 × 25 mesh.*

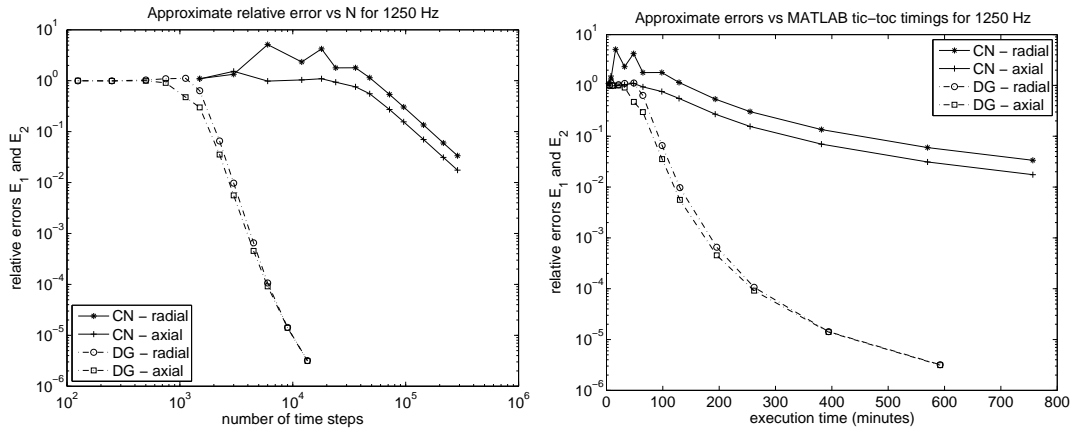
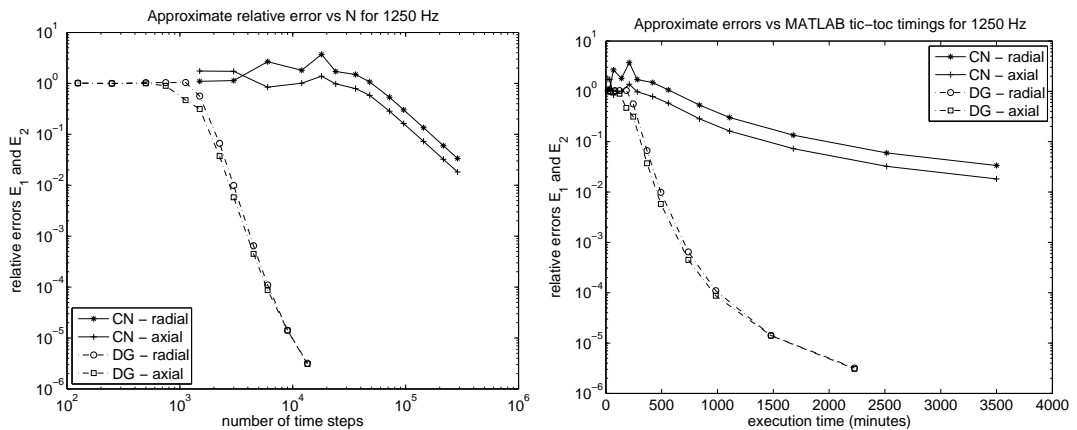


Figure 35: *Approximated errors and 'tic-toc' MATLAB [®] timings in minutes for the 1250 Hz run with CN and DG(3) on a 25 × 50 mesh.*



our attention to a two-dimensional meridian-plane cross section: we take $\Omega = \{0.00175 < r < 0.027\} \text{ m} \times \{0 < z < 0.0514\} \text{ m}$ and we set $T = 0.5$ seconds.

The bottom of the cylinder is assumed fixed in both coordinate directions (a homogeneous Dirichlet boundary condition) while the outer radius and top are stress free (a homogeneous Neumann boundary condition). The inner radius is subject to an oscillating traction $\mathbf{g}(t) = (0, g(t))^T$ where,

$$g(t) = 500 \text{ramp}(t) \sin(2\pi ft) \exp(-100,000(z - \bar{z})^2) \quad (25)$$

for $\bar{z} = 0.0257$ and with a frequency, f , as specified below (we hope that the use of f here as a frequency, and earlier as a load, will not create any confusion). Here,

$$\text{ramp}(t) = \begin{cases} \sin^2\left(\frac{\pi ft}{100}\right) & \text{if } t < 50/f; \\ 1 & \text{otherwise,} \end{cases}$$

is a ‘ramp-up’ function the role of which is to ensure that high frequency noise associated with sudden starts does not pollute the signal — this ramp allows for the full amplitude of the traction to develop slowly over 50 full cycles. This is intended to mimic the experimental set-up.

The material data are taken as $\rho = 1010 \text{ kg/m}^3$, $E_0 = 167 \text{ kPa}$ and $\nu = 0.44$ (the Voigt term was set to zero: $\mathbf{C} = \mathbf{0}$). High quality estimates for the viscoelastic parameters will soon appear in [5] but for the sake of illustration here we simply took $\varphi_0 = 0.2$, $\varphi_1 = 0.8$ and $\tau_1 = 2$ with $N_\varphi = 1$ in (16). The spatial discretization used below is a SEM on, mostly, a 13 (radial) by 25 (axial) uniform mesh of bicubics supported on tensor products of the Gauss-Lobatto nodes. (We also ran some problems on a 25 by 50 mesh, and will return to this point later.) The DG time discretization used piecewise cubic polynomials (we refer to this as ‘DG(3)’ below) and all except for the spectral quadratures (the mass and stiffness matrices) use high order (degree 12 in space and time) Gauss-Legendre rules to calculate the (space and time) definite integrals.

The imposed traction, \mathbf{g} , in (25) simulates the wall shear disturbance that may arise from a diseased (stenosed) artery, represented by the centre line of the cylinder, and in order to illustrate the performance of the DG-in-time method as developed above we report here on the resultant displacement signals computed at the point $\mathcal{O} = (r, z) = (0.027, 0.01028)$ on the outer surface. This models a diagnostic sensor location on the chest surface.

For the $\{250, 500, 750, 1000, 1250\}$ Hz family of frequencies we compare the performance of the DG method against the more standard CN method. In the computations that follow we took

$$N_{CN} \in \{1500, 3000, 6000, 12000, 18000, 24000, 36000, 48000, 72000, \\ 96000, 144000, 216000, 288000\}$$

time steps for the CN method and

$$N_{DG} \in \{125, 250, 500, 750, 1125, 1500, 2250, 3000, 4500, 6000, 9000, 13500, 18000\}$$

time steps for DG(3). The larger numbers were not used for the lower frequencies. The timing figures are based on using MATLAB’s $\text{\textcircled{R}}$ `tic` and `toc` commands (the entire code is

currently prototyped in MATLAB [®]). Also, if we take N time steps up to time $T = 0.5$ to simulate a signal with a frequency, f , as given earlier then we have $2N/f$ time steps per wave. Thinking about the the minimum number of data points we need to represent such a wave we see that we must have $2N_{CN}/f \geq 4$, to get five data points per wave, and $2N_{DG}/f \geq 1$ to get one cubic polynomial per wave. It follows that the minimum number of time steps for each given frequency is then,

$$\begin{aligned} N_{CN} &= 2\{250, 500, 750, 1000, 1250\} = \{500, 1000, 1500, 2000, 2500\} \\ N_{CN} &= \{250, 500, 750, 1000, 1250\}/2 = \{125, 250, 375, 500, 625\}. \end{aligned}$$

Selections from the computed signals are shown for $f = 250$ Hz and a 25×50 mesh in Figure 22, and for a 13×25 mesh in Figure 23, For a 13×25 mesh the output for $f = 500$ Hz is in Figure 24, for $f = 750$ Hz in Figure 25, and, for $f = 1000$ Hz in Figure 26, For $f = 1250$ Hz selected output is shown in Figure 27, for the 13×25 mesh while for the 25×50 mesh we show output in Figure 28,

6 Conclusions and discussion

The results for the 1D problems in Examples 1, 2, 3 and 4 show the behaviour of ‘time error’ in the computed solution for four cases covering elasticity and mixtures of viscoelastic formulations. Since Examples 1 and 4 were similar, and Examples 2 and 3 were also similar we can infer that the presence of Maxwell-Zener viscoelasticity does not alter the convergence properties of the scheme away from that displayed by the standard wave equation. The addition of a Kelvin-Voigt term, however, does seem to negatively affect the convergence behaviour.

In particular, for Examples 1 and 4, from Figure 2 we can infer Crank-Nicolson convergence with energy error like k^2 , DG(1) like k^3 , DG(2) like k^5 , DG(3) like k^7 . It seems safe to conjecture a DG(r) energy error of order $O(k^{2r+1})$.

On the other hand, for Examples 2 and 3, from Figure 1 we can infer that the Crank-Nicolson scheme converges with energy error like k^2 and the linear DG scheme with energy error like k^3 . These are as expected. However, the quadratic and cubic DG schemes seem to converge like $k^{4.5}$ and k^6 while the quartic and and quintic seem both to be between k^7 and k^8 . The sextic and septic schemes appear to converge with at least k^9 . The reason for these unexpected behaviours is not clear although we suspect that the precision of the computations is inadequate for these high order approximations. It does, however, seem safe to conclude that convergence is not so rapid when a Kelvin-Voigt term is present.

The accompanying work-error plots seek to illustrate the efficiency associated with higher order methods. However, they need to be interpreted with care since it would be unlikely to have only ‘time error’ in a problem of real interest. They are included merely to remind us that the extra linear algebra workload must be borne in mind when decoupling in time. These results were for the Galerkin-in-space method. The results for the spectral element method were similar in both cases.

To discuss space-time convergence we moved on to consider problems in two space dimensions, beginning with the scalar wave equation in Examples 5 and 6.

First, for Example 5 we infer from Figure 3 that $\|u(t_N) - U_N^-\|_{L_2(\Omega)} = O(h^{d+1} + k^{d+2})$ for the Galerkin-in-space scheme, with the last term being suggested by the bottom table in the figure. In a similar way, Figure 4 suggests that $\|\nabla u(t_N) - \nabla U_N^-\|_{L_2(\Omega)} = O(h^d + k^{d+1})$, although the last term is not so clearly apparent in this case. The results for $w = \dot{u}$ are not so useful. The curves in Figure 5 quite clearly show rapid convergence as the order increases but the tables do not give useful figures. The convergence behaviour seems too erratic to be able to draw useful conclusions. Figures 6, 7 and 8 show analogous results for the spectral element scheme in the case where equal degrees are used in space and time. The same conclusions can be drawn as for the Galerkin scheme.

Example 6 has different types of boundary data. Figures 9, 10 and 11 for the Galerkin-in-space scheme with Figures 12, 13 and 14 for the spectral element scheme suggest essentially the same behaviour as for Example 5.

We then moved on to consider an example in viscodynamics in Example 7. Figures 15, 16 and 17 for the Galerkin-in-space scheme and Figures 18, 19 and 20 for the spectral element scheme are compatible with the expectations of error rates indicated by Examples 5 and 6. For that reason we did not pursue a more extensive numerical study of convergence in this case.

While these rates of convergence are, broadly, in line with what we might expect we should sound a note of caution. A single discretization parameter, N , has been used which means that the mesh width and time steps are, in essence, the same. The mixing of h and k as suggested by Johnson's results (see earlier in (4) and (5)) will therefore not be clearly revealed in our study. Also, curiously, we did not clearly observe the semi-integer rate predicted by Johnson's bounds, although it is possible that this is 'hidden' in the quite ragged results for w .

We now move on to consider the results from the practical example in Section 5. Beginning with the computations for the least challenging frequency, 250 Hz, we see output results for a selection of time step sizes and for the 25×50 spatial mesh in Figure 22. The corresponding results for the 13×25 mesh are shown in Figure 23 (note that animated results demonstrating temporal convergence in the electronic PDF of [34]).

In a crude 'eyeball judgement' we can see that the DG(3) scheme seems to have converged to a practically useful level of accuracy, and with both meshes, at 500 time steps whereas CN requires around 12000 for both meshes. This equates to 2000 complex system solves for DG(3) as against 12000 real solves for CN.

We can use this observation to infer that it is reasonable to assume that the DG solution for the largest N_{DG} is much more accurate than the CN solution at all considered values of N_{CN} . This suggests a method for approximating the error in these computed signals. For each of the frequencies we take the DG solution corresponding to the largest N_{DG} in use, call these $\tilde{\mathbf{u}}$ and $N_{DG,\max}$, and assume that it is 'exact'. We then approximate the error in the CN and DG solutions on the set, \mathbb{S} , of discrete times that are common to the 'exact' computation and the one being assessed. With these notions we define the relative radial (subscript $j = 1$) and axial (subscript $j = 2$) errors by,

$$E_j := \frac{\max \left\{ |\tilde{u}_j(t_i) - u_j(t_i)| : i \in \mathbb{S} \right\}}{\max \left\{ |\tilde{u}_j(t_i)| : 1 \leq i \leq N_{DG,\max} \right\}}.$$

The results are shown in Figures 29 and 30 for the 24×50 mesh and the 13×25 mesh. We can see that they are effectively identical and, of course, we caution against paying too much attention to the estimated relative errors associated with the larger values of N_{DG} . We also recorded the run times using MATLAB's $\text{\textcircled{R}}$ `tic` and `toc` commands and although this allows the execution times to be plotted against number of time steps we consider it more interesting to plot error as a function of execution time.

Here, for the 25×50 computation we see from the left of Figure 29 that to obtain a relative error of about 10^{-3} we need around 500 DG(3) steps and 48000 CN steps. The right hand plot tells us that, for these values, CN took about 400 minutes: about ten times that of DG(3).

Since Figure 29 and Figure 30 are essentially the same (except, of course, for execution time) we can assume that we have in effect computed an 'exact solution' which gives us confidence in our findings at 250 Hz. Moving on to the higher frequencies we have for the 13×25 mesh selected results for:

- 500 Hz in Figure 24 and timings and estimated errors in Figure 31. We infer convergence for DG(3) by 1500 time steps and for CN by 48000;
- 750 Hz in Figure 25 and timings and estimated errors in Figure 32. Convergence seems here to have occurred for DG(3) by 2250 and for CN by 96000;
- 1000 Hz in Figure 26 and timings and estimated errors in Figure 33. In this case it seems as though DG(3) needs only 3000 steps while CN required 144000.

We have to be cautious about placing too much trust in the error plots in Figures 31, 32 and 33, because we did not perform a duplicate run on a 25×50 mesh and so cannot be sure that we have a meaningful 'exact' solution. To illustrate this we now give the results for the much more challenging highest frequency, 1250 Hz, that we computed for.

For the 13×25 mesh we show selected results in Figure 27. The corresponding 25×50 mesh results are in Figure 28. The error and timing data are shown in Figure 34 for the 13×25 mesh and in Figure 35 for the 25×50 mesh.

It seems clear that on the 13×25 mesh the DG(3) results have converged by 3000 time steps and CN by 288,000 while for the 25×50 mesh we would estimate these figures at 4500 and 288,000. However, the 'converged plots' are not the same — there are significant differences in the wave envelopes for times later than 0.2. This is a clear indication that a finer spatial mesh is needed in order to properly assess the situation at higher frequencies. This study is ongoing but will have to wait for a software development phase to be completed: the execution times required by MATLAB $\text{\textcircled{R}}$ for repeating all these tests on a, say, 50×100 mesh, are prohibitive.

In closing we remark that, despite the need to introduce complex arithmetic, it seems clear that DG(3) and, by extension, DG(p), can offer much greater efficiency for certain types of wave equation problem. Linearity, solution smoothness and (temporally) constant coefficients are the obvious desirable properties, and we note that in engineering dynamics these are often satisfied. The extension and study of the technique beyond these assumptions seems worthwhile, as does a full and detailed *a priori* error analysis building on that in [33]. Based on the results above we could conjecture a temporal convergence rate at the nodes

corresponding to a $O(k^{2q+1})$ error term (as for the DG scheme for parabolic problems in [18]) when the Kelvin-Voigt term is not present. It also seems clear that the addition of Maxwell-Zener viscoelastic damping does not affect the convergence rates.

In closing we note that the scheme developed above is suited to both coarse and fine grained parallelism, and a continuous Galerkin decoupling analogue should also be possible, as for the heat equation in [35].

References

- [1] M. Ainsworth, P. Monk, and W. Muniz. Dispersive and dissipative properties of discontinuous Galerkin finite element methods for the second-order wave equation. *Journal of Scientific Computing*, 27:5–40, 2006.
- [2] Mark Ainsworth and Hafiz Abdul Wajid. Optimally blended spectral-finite element scheme for wave propagation and nonstandard reduced integration. *SIAM J. Numer. Anal.*, 48(1):346–371, 2010.
- [3] W. Bangerth and R. Rannacher. Finite element approximation of the acoustic wave equation: error control and mesh refinement. *East-West J. Numer. Math.*, 7(4):263–282, 1999. ganymed.iwr.uni-heidelberg.de/Paper/Preprint1999-15.pdf.
- [4] H T Banks, Shuhua Hu, Zackary R Kenz, Carola Kruse, Simon Shaw, John R Whiteman, Mark Brewin, Stephen E Greenwald, and Malcolm Birch. Material parameter estimation and hypothesis testing on a 1D viscoelastic stenosis model: methodology. *J. Inverse Ill-Posed Probl.*, 21:25–57, 2013. doi: 10.1515/jip-2012-0081; BURA: TBC; (BICOM Tech. Rep. 13/1, see www.brunel.ac.uk/bicom).
- [5] H T Banks, Shuhua Hu, Zackary R Kenz, Carola Kruse, Simon Shaw, John R Whiteman, Mark Brewin, Stephen E Greenwald, and Malcolm Birch. Model validation for a noninvasive arterial stenosis detection problem. Accepted with revisions: Mathematical Biosciences and Engineering. doi: TBC; BURA: TBC; (BICOM Tech. Rep. 13/2, see www.brunel.ac.uk/bicom), (expected 2013).
- [6] H.T. Banks, J.H. Barnes, A. Eberhardt, H. Tran, and S. Wynne. Modeling and computation of propagating waves from coronary stenoses. *Comp. and Appl. Math.*, 21:767–788, 2002. Tech. Rep. CRSC-TR00-20 at www.ncsu.edu/crsc/reports.html.
- [7] H.T. Banks and J.R. Samuels Jr. Detection of arterial occlusions using viscoelastic wave propagation. *Adv. Appl. Math. Mech.*, 1:1–28, 2009.
- [8] Jonás D. De Basabe, Mrinal K. Sen, and Mary F. Wheeler. The interior penalty discontinuous Galerkin method for elastic wave propagation: grid dispersion. *Geophys J. Int.*, 175:83–93, 2008.
- [9] Stephan Baumüller, Sebastian Leschka, Lotus Desbiolles, Paul Stolzmann, Hans Scheffel, Burkhardt Seifert, Borut Marincek, and Hatem Alkadhi. Dual-source versus 64-section ct coronary angiography at lower heart rates: Comparison of accuracy and radiation dose. *Radiology*, 253(1):56–64, 2009.

- [10] Ted Belytschko and R. Mullen. On dispersive properties of finite element solutions. In Julius Miklowitz and Jan D. Achenbach, editors, *Proceedings of modern problems in elastic wave propagation*, pages 67—82. Wiley, 1978. Symposium held at Northwestern University, USA, Sept. 12–15, 1977.
- [11] Mark Brewin, Stephen E Greenwald, Malcolm Birch, Carola Kruse, Simon Shaw, John R Whiteman, H T Banks, Shuhua Hu, and Zackary R Kenz. Characterization of the uniaxial elastic properties of an agar-based tissue mimicking material. In preparation.
- [12] G. F. Carey and E. Barragy. Basis function selection and preconditioning high degree finite element and spectral methods. *BIT*, 29:794—804, 1989.
- [13] M. J. S. Chin-Joe-Kong, W. A. Mulder, and M. van Veldhuizen. Higher-order triangular and tetrahedral finite elements with mass lumping for solving the wave equation. *Journal of Engineering Mathematics*, 35:405—426, 1999.
- [14] Jintai Chung and Gregory M. Hulbert. A family of single-step Houbolt time integration algorithms for structural dynamics. *Comput. Methods Appl. Mech. Engrg.*, 118:1—11, 1994.
- [15] G. Cohen, P. Joly, J. E. Roberts, and N. Tordjman. Higher order triangular finite elements with mass lumping for the wave equation. *SIAM J. Numer. Anal.*, 38:2047—2078, 2001.
- [16] R. Courant. Variational methods for the solution of problems of equilibrium and vibrations. *Bull. Am. Math. Soc*, 49:1—23, 1943.
- [17] M. Duruffe, P. Grob, and P. Joly. Influence of Gauss and Gauss-Lobatto quadrature rules on the accuracy of a quadrilateral finite element method. *Numer. Methods Partial Differential Equations*, 25:526—551, 2009. DOI 10.1002/num.20353.
- [18] Kenneth Eriksson and Claes Johnson. Adaptive finite element methods for parabolic problems. I: a linear model problem. *SIAM J. Numer. Anal.*, 28:43—77, 1991.
- [19] J. D. Ferry. *Viscoelastic properties of polymers*. John Wiley and Sons Inc., 1970.
- [20] Donald A. French. A space-time finite element method for the wave equation. *Comput. Methods Appl. Mech. Engrg.*, 107:145—157, 1993.
- [21] Donald A. French and Todd E. Peterson. A continuous space-time finite element method for the wave equation. *Math. Comput.*, 65:491—506, 1996.
- [22] Y.C. Fung. *Biomechanics: mechanical properties of living tissues*. Springer-Verlag New York Inc., 1993.
- [23] J. M. Golden and G. A. C. Graham. *Boundary value problems in linear viscoelasticity*. Springer-Verlag, 1988.
- [24] Roland Griesmaier and Peter Monk. Discretization of the wave equation using continuous elements in time and a hybridizable discontinuous Galerkin method in space. In Review.

- [25] B. T. Helenbrook. On the existence of explicit hp -finite element methods using Gauss-Lobatto integration on the triangle. *SIAM J. Numer. Anal.*, 47:1304—1318, 2009.
- [26] Thomas J. R. Hughes and Gregory M. Hulbert. Space-time finite element methods for elastodynamics: formulations and error estimates. *Comp. Meth. Appl. Mech. Eng.*, 66:339—363, 1988.
- [27] Gregory M. Hulbert and Thomas J. R. Hughes. Space-time finite element methods for second-order hyperbolic equations. *Comp. Meth. Appl. Mech. Eng.*, 84:327—348, 1990.
- [28] B. L. Hulme. Discrete Galerkin and related one-step methods for ordinary differential equations. *Math. Comp.*, 26:881—891, 1972.
- [29] B. L. Hulme. One-step piecewise polynomial Galerkin methods for initial value problems. *Math. Comp.*, 26:415—426, 1972.
- [30] A. R. Johnson. Modeling viscoelastic materials using internal variables. *The Shock and Vibration Digest*, 31:91—100, 1999.
- [31] A. R. Johnson, A. Tessler, and M. Dambach. Dynamics of thick viscoelastic beams. *Journal of Engineering Materials and Technology*, 119:273—278, 1997.
- [32] Claes Johnson. *Numerical solution of partial differential equations by the finite element method*. Cambridge University Press, Cambridge, 1987.
- [33] Claes Johnson. Discontinuous Galerkin finite element methods for second order hyperbolic problems. *Comp. Meth. Appl. Mech. Eng.*, 107:117—129, 1993.
- [34] Carola Kruse, Matthias Maischak, Simon Shaw, John R Whiteman, Stephen E Greenwald, Malcolm J Birch, Mark P Brewin, H T Banks, Zackary R Kenz, and Shuhua Hu. High order space-time finite element schemes for acoustic and viscodynamic wave equations with temporal decoupling. In preparation. Technical Report 13/5, www.brunel.ac.uk/bicom.
- [35] Carola Kruse and Simon Shaw. Time-decoupled high order continuous space-time finite element schemes for the heat equation. Submitted to SIAM J. Scientific Computing. Technical Report 13/7, www.brunel.ac.uk/bicom.
- [36] X. D. Li and N.-E. Wiberg. Implementation and adaptivity of a space-time finite element method for structural dynamics. *Comput. Methods Appl. Mech. Engrg.*, 156:211—229, 1998.
- [37] F. J. Lockett. *Nonlinear viscoelastic solids*. Academic Press, 1972.
- [38] Ilario Mazzieri and Francesca Rapetti. Dispersion analysis of triangle-based spectral element methods for elastic wave propagation. *Numer. Algor.*, 60:631—650, 2012.
- [39] Béatrice Rivière, Simon Shaw, and J.R. Whiteman. Discontinuous Galerkin finite element methods for dynamic linear solid viscoelasticity problems. *Numer. Methods Partial Differential Equations*, 23:1149—1166, 2007. See also report 05/7 at www.brunel.ac.uk/bicom.

- [40] John Semmlow and Ketaki Rahalkar. Acoustic detection of coronary artery disease. *Annu. Rev. Biomed. Eng.*, 9:449—469, 2007.
- [41] Simon Shaw and J. R. Whiteman. Numerical solution of linear quasistatic hereditary viscoelasticity problems. *SIAM J. Numer. Anal.*, 38(1):80—97, 2000.
- [42] M. J. Turner, R. W. Clough, H. C. Martin, and L. J. Topp. Stiffness and deflection analysis of complex structures. *J. Aero. Sci.*, 23:805—823, 1956.
- [43] T. Werder, K. Gerdes, D. Schötzau, and C. Schwab. *hp*-discontinuous Galerkin time stepping for parabolic problems. *Comput. Methods Appl. Mech. Engrg.*, 190:6685—6708, 2001.
- [44] J. Wloka. *Partial Differential Equations*. Cambridge University Press, 1987.
- [45] Yuan Xu. On Gauss-Lobatto integration on the triangle. *SIAM J. Numer. Anal.*, 49:541—548, 2011.
- [46] O. C. Zienkiewicz. A new look at the Newmark, Houbolt and other time stepping formulas. A weighted residual approach. *Earthquake Engineering and Structural Dynamics*, 5:413—418, 1977.